

411 **Chapter 3**

412 **Gravity inversion: a tool for**
413 **bathymetry modelling**

414 **Abstract**

415 Sub ice-shelf bathymetry exerts a primary control on the stability of many Antarctic
416 ice shelves through the geometry of pinning points and the guiding of melt-inducing
417 water masses. Collecting sub-ice shelf bathymetry data using typical polar surveying
418 methods (e.g. seismic surveying or direct observations) can be inefficient, expensive
419 or unfeasible. Gravity inversions provide a more practical alternative, in which ob-
420 served variations in Earth's gravitational field are used to predict the bathymetry.
421 This chapter describes a gravity inversion algorithm developed specifically for mod-
422 elling bathymetry. The inversion is tested on a suite of models, created with a
423 combination of synthetic and real topographic data. These tests provide the ability
424 to 1) determine the best practises for conducting bathymetric inversions, 2) recog-
425 nize limitations of the inversions, and 3) identify where community efforts should
426 be focused for the future of modelling Antarctica's sub ice shelf bathymetry.

427 **3.1 Introduction**

428 In the last two decades, the Antarctic Ice Sheet has experienced significant ice mass
429 loss, averaging 118 billion tons per year, contributing 5.2mm to sea-level rise (B.
430 Smith et al., 2020). This mass loss has been concentrated along the coast, where
431 ocean currents are able to bring warm waters in contact with the ice (Rignot et al.,
432 2019). Much of Antarctica is fringed with floating extensions of the ice sheet, known
433 as ice shelves (Figure 3.1). These ice shelves provide a critical buttressing effect on
434 the upstream ice, slowing the flow of ice from the continent into the oceans (Dupont
435 & Alley, 2005). This buttressing largely results from friction between the ice and
436 the bed along the grounding zone. While this friction would still exist without the
437 ice shelf, the presence of the shelf distributes these restraining forces to other areas
438 of the grounding zone, where friction may be low, such as fast-moving ice streams
439 (Goldberg, 2017). Thinning of the ice shelves lowers the amount of ice-bed contact
440 along the grounding zone, reducing this buttressing effect. Due to the cold climate
441 and lack of surface melt, the majority of Antarctic ice shelves' thinning occurs as
442 basal melt. This basal melt (Figure 3.1b) occurs from contact with relatively warm
443 ocean waters, such as circumpolar deep water and high-salinity shelf water (CDW

and HSSW) (Jenkins et al., 2010; Rignot et al., 2019).

These deep-lying warm masses of water originate offshore from the ice shelves and thus can only induce basal melting if they circulate under the shelves. A large enough ocean draft, the distance between the ice base and the bathymetry (Figure 3.1a), is required for this circulation to be possible. This connection between ocean draft and basal melting is shown by generally low ice shelf basal melt rates for shelves, or sections of shelves, with shallow ocean drafts (e.g. Pritchard et al., 2012; Tinto et al., 2019). Additionally, deep bathymetric troughs in regions of otherwise thin drafts, or conversely, bathymetry ridges in regions of thick drafts, can control the incursion of these water masses (St-Laurent et al., 2013; Yang et al., 2021).

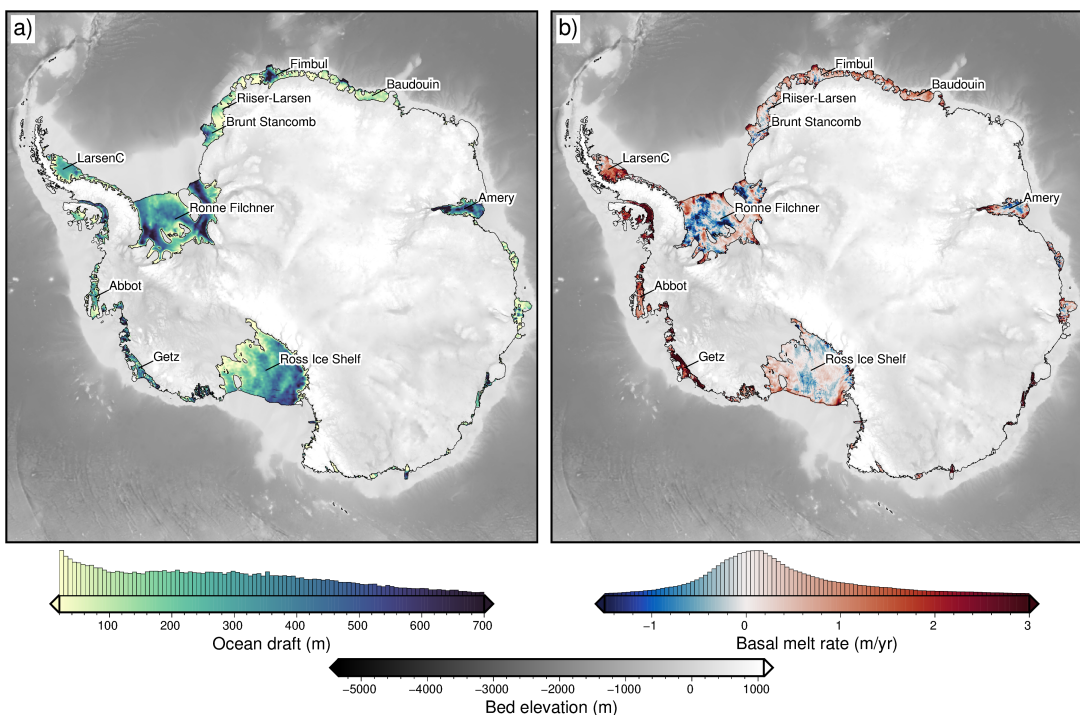


Figure 3.1: Ice shelves of Antarctica. **a)** Water column thickness beneath the ice shelves from BedMachine data (Morlighem et al., 2020). **b)** Basal melt rate for the ice shelves from Adusumilli et al. (2020). Both plots show bed elevations in the gray colormap. 10 largest ice shelves are labeled.

While the elevation of the ice base for many of Antarctic's ice shelves is relatively well constrained, the water depth is poorly known. The relatively good understanding of the ice base comes from a combination of airborne radar surveys (e.g. Das et al., 2020) and satellite altimetry measurements (e.g. Griggs & Bamber, 2011), in conjunction with the hydrostatic equilibrium assumption (Bamber & Bentley, 1994). Conversely, there is no equivalent fast and cheap technique to directly survey the bathymetry beneath floating ice shelves. Radar (ground or airborne) cannot image through the thick water, over-ice seismic surveys are slow and expensive, and numerous direct observations through drill holes are impractical. Due to the density contrast between the water and the sediment, the bathymetry surface produces a measurable gravity signal. This signal can be observed from airborne or ground-based gravity surveys, which provides a method, if used correctly, to model sub-shelf bathymetry. This method is a gravity inversion; a geophysical technique to take measurements of an energy source and estimate the physical properties responsible for these measurements (Oldenburg & Li, 2005). In this case, the energy

source is Earth's gravitational field and the physical earth property is the depth of the density contrast between the ocean and seafloor. This chapter will first introduce the gravity inversion technique in general, followed by the specific style of gravity inversion, a geometric inversion, which is used here. Next, a suite of synthetic models will be used to assess the performance and limitation of the inversion. The suite of models includes:

1. a simple synthetic topography.
2. a synthetic topography with a regional component of the gravity signal.
3. a semi-realistic model, using real Antarctic bathymetry and basement topographies to create the synthetic observed gravity.

With this suite of models, we will test the effects of various levels of noise, the data spacing of the observed gravity, the number of prior constraints, and various inversion methods and parameters. Final, we will discuss the general limitations of using gravity inversions to recover bathymetry, and will provide guidance for conducting gravity inversion for sub ice shelf bathymetry.

3.2 Methods

There are two fundamental types of geophysical modelling, forward modelling and inverse modelling. Forward modelling is the process of simulating observed data from a model of physical properties. For a gravity application, this may be calculating the gravitational field resulting from a sedimentary basin. In general, forward problems are well-posed, meaning there is a unique answer (Oldenburg & Li, 2005). In contrast, inverse modelling, or inversion, is the process of determining physical properties from observed data. For the previous example, this would entail using observed gravity data to predict the sediment thickness of a basin. Inverse problems are generally ill-posed. For a given set of gravity observations, there are a multitude of sedimentary basin configurations which reproduce the observed data equally well. This is referred to as non-uniqueness and makes geophysical inversions a difficult procedure compared to forward modeling.

3.2.1 Geophysical inversion

In general, inversions consist of three components;

1. Forward operator (f): This is a mathematical means of linking a physical Earth property to the expected geophysical response. It accomplishes the task of forward modelling, as described above.
2. Physical property model (p): This is a representation of the physical Earth property of interest. While real-world properties are continuous (i.e. a smoothly varying topography), computation often necessitates discretization (i.e. a DEM (digital elevation model), see section 3.2.2). The starting model (p_0) typically will include the prior geologic knowledge of the region.
3. Fit function (ϕ): This function describes the similarity between the observed data and the predicted data (resulting from the forward calculation of the

509 property model ($f(p)$)). The goal of the inversion is to minimize this function,
 510 so that $f(p)$ is as close to the observed data as possible.

511 Here, a mathematical derivation of a generalized inversion problem is shown,
 512 following closely to the derivation of Oliveira and Uieda (2014). The inversion
 513 problem can be framed as finding the set of physical parameters (\vec{p}) which when
 514 modeled with the forward operator (f) produce predicted data (\vec{d}^{pred}) as close to
 515 the observed data (\vec{d}^{obs}), as possible. The difference between the observed and
 516 predicted data gives the misfit \vec{m} , where

$$\vec{m} = \vec{d}^{obs} - \vec{d}^{pred} = \vec{d}^{obs} - f(\vec{p}). \quad (3.1)$$

517 Here, the squared ℓ^2 -norm (mean squared error) of the misfit is the metric used
 518 to define the *closeness* between the predicted and observed data, where

$$\|\vec{m}\|_2^2 = \sum_{i=1}^N [d_i^{obs} - f_i(\vec{p})]^2. \quad (3.2)$$

519 This is defined as the *fit function*, $\phi(\vec{p})$. The fit function can also be expressed
 520 as

$$\phi(\vec{p}) = \vec{m} \cdot \vec{m} = \vec{m}^T \vec{m} = [\vec{d}^{obs} - f(\vec{p})]^T [\vec{d}^{obs} - f(\vec{p})]. \quad (3.3)$$

521 In this context, the inversion problem is to determine a vector of parameters
 522 \tilde{p} which minimizes $\phi(\vec{p})$. This minimum occurs where the gradient of $\phi(\vec{p})$ at
 523 the vector \tilde{p} has zero-length. The gradient of $\phi(\vec{p})$ evaluated at any \vec{p} is an M-
 524 dimensional vector is defined as

$$\nabla \phi(\vec{p}) = \begin{bmatrix} \frac{\partial \phi(\vec{p})}{\partial p_1} \\ \frac{\partial \phi(\vec{p})}{\partial p_2} \\ \vdots \\ \frac{\partial \phi(\vec{p})}{\partial p_M} \end{bmatrix}. \quad (3.4)$$

525 Evaluating the gradient at the i-th element, using equation 3.3 gives

$$\begin{aligned} \frac{\partial \phi(\vec{p})}{\partial p_i} &= \frac{\partial}{\partial p_i} \left\{ [\vec{d}^{obs} - f(\vec{p})]^T [\vec{d}^{obs} - f(\vec{p})] \right\} \\ &= \left\{ - \frac{\partial f(\vec{p})^T}{\partial p_i} [\vec{d}^{obs} - f(\vec{p})] \right\} + \left\{ - [\vec{d}^{obs} - f(\vec{p})]^T \frac{\partial f(\vec{p})}{\partial p_i} \right\} \end{aligned} \quad (3.5)$$

526 which, since the transpose of a scalar is equal to itself, is simplified to

$$\frac{\partial \phi(\vec{p})}{\partial p_i} = -2 \frac{\partial f(\vec{p})^T}{\partial p_i} [\vec{d}^{obs} - f(\vec{p})]. \quad (3.6)$$

527 Substituting equation 3.6 into the equation 3.4 and simplifying gives

$$\nabla\phi(\vec{p}) = -2\mathbb{J}(\vec{p})^T[\vec{d}^{obs} - f(\vec{p})] \quad (3.7)$$

528 where the matrix $\mathbb{J}(\vec{p})$ has dimensions $N \times M$ and is the *Jacobian matrix* of
 529 $f(\vec{p})$.

$$\mathbb{J}(\vec{p}) = \begin{bmatrix} \frac{\partial \vec{f}(\vec{p})}{\partial p_1} & \frac{\partial \vec{f}(\vec{p})}{\partial p_2} & \dots & \frac{\partial \vec{f}(\vec{p})}{\partial p_M} \end{bmatrix} = \begin{bmatrix} \frac{\partial f_1(\vec{p})}{\partial p_1} & \frac{\partial f_1(\vec{p})}{\partial p_2} & \dots & \frac{\partial f_1(\vec{p})}{\partial p_M} \\ \frac{\partial f_2(\vec{p})}{\partial p_1} & \frac{\partial f_2(\vec{p})}{\partial p_2} & \dots & \frac{\partial f_2(\vec{p})}{\partial p_M} \\ \vdots & \vdots & \ddots & \vdots \\ \frac{\partial f_N(\vec{p})}{\partial p_1} & \frac{\partial f_N(\vec{p})}{\partial p_2} & \dots & \frac{\partial f_N(\vec{p})}{\partial p_M} \end{bmatrix}. \quad (3.8)$$

530 The *Jacobian* (\mathbb{J}) is a sensitivity matrix. Each row represents an element of
 531 the predicted data and each column represent an element of the physical parameter
 532 vector (\vec{p}). Each entry is the partial derivative of the predicted data with respect
 533 to the physical parameter. For example, lets consider the case of a gravity inversion
 534 attempting to recover the density of subsurface cubes. The model consists of 100
 535 cubes, and there are 10 observation points. The Jacobian would be a 10×100 matrix
 536 where $\mathbb{J}_{1,1}$ (the first entry) would be the 1st cube's gravitational derivative with
 537 respect to density at the first observation point. The Jacobian therefore describes
 538 how sensitive each pair of cubes and observations are to a change in density.

539 Once the Jacobian is created, a matrix equation of the form $Ax = b$ is set up,
 540 where A is the Jacobian, b is the data misfit, and x is the unknown variable.

$$\mathbb{J}\vec{x} = \vec{m} \quad (3.9)$$

541 A solution to this equation can be found with an iterative least-squares solver. The
 542 solution gives the correction to the physical parameters of interest which minimizes
 543 the misfit between the observed data and the starting model. For certain types
 544 of inversions it is necessary to repeat the entire inversion process several times, as
 545 explained below.

546 Non-Linear inversions

547 The derivative of the forward operator with respect to the parameter of interest
 548 determines the linearity of an inversion. For a gravity inversion attempting to recover
 549 rock density, the derivative of gravity with respect to density is linear, and thus the
 550 inversion is considered linear (Aster et al., 2018). Conversely, a gravity inversion
 551 attempting to recover the depth to a surface, or the thickness of a layer, is non-
 552 linear, since the vertical derivative of gravity (derivative with respect to depth) is a
 553 non-linear function. Non-linear inversions are similar to linear ones, with the added
 554 necessity to run the inversion iteratively. This is to avoid issues regarding multiple
 555 minima of the gradient of the fit function ($\nabla\phi(\vec{p})$) (Oliveira & Uieda, 2014). For
 556 multiple iterations, the calculated corrections (\vec{x}) are applied to the starting model,
 557 the residuals (\vec{m}) are recalculated, the Jacobian is updated, and equation 3.9 is
 558 solved again, giving a new set of corrections. This is repeated until $\phi(\vec{p})$ is suitably
 559 low.

560 **Geometric inversions**

561 Most gravity inversions aim to recover the distributions of densities in the subsurface.
 562 For this technique, the model domain is discretized into a series of polygons (for
 563 2D) or polyhedrons (for 3D), and the inversion aims to predict the density of each
 564 polygon. This is widely used due to it's relevance in mineral exploration (Oldenburg
 565 & Pratt, 2007). Less commonly used are gravity inversions which aim to recover
 566 the depth, shape or volume of features. This style of gravity inversions are referred
 567 to as geometric inversions. They are typically used to estimate relief of the Moho
 568 (e.g Borghi, 2022; Uieda & Barbosa, 2017) or the sediment-basement contact (e.g.
 569 Barbosa et al., 2007; Santos et al., 2015). In this chapter geometric inversions
 570 are used to recover the bathymetry. This use case of gravity inversion is unique
 571 to studying the cryosphere. In locations without ice cover, bathymetry data is
 572 typically collected with shipborne multi-beam echo sounding, airborne LiDAR, or
 573 satellite altimetry.

574 **3.2.2 Forward modelling**

575 To perform a geometric gravity inversion, first the gravitational field produced by a
 576 topographic surface must be able to be calculated. This topography is approximated
 577 as a constant density contrast between the overlying and underlying materials. The
 578 topography is modeled as a series of adjacent vertical right-rectangular prisms. For
 579 a certain observation point, the gravitational field produced by this layer of prisms
 580 is the sum of the forward gravity of each prism. This forward gravity calculation of
 581 a prism is accomplished with the analytical solutions given by Nagy et al. (2000),
 582 as implemented in the Python package Harmonica (Project et al., 2023).

583 **Discretization**

584 There are several options for discretizing a density contrast as a series of prisms
 585 (Figure 3.2). The most conceptually simple method is for the prisms to represent
 586 the true density and geometry of the material on either side of the surface (Figure
 587 3.2b). If this method, the topography is represented by the base of the above prisms,
 588 and by the tops of the lower prisms. Alternatively, the contrast can be represented by
 589 a layer of prisms either above or below the surface, ending at an arbitrary reference,
 590 typically the minimum or maximum value of the surface (Figure 3.2c-d). For this,
 591 the prism's density values are relative to the medium on the other side of the surface
 592 (i.e. if prisms are below the surface, their densities are $\rho_{below} - \rho_{above}$). The last option
 593 is to choose a flat reference surface (typically the mean value of the surface or sea-
 594 level) and create prisms between this and the surface (Figure 3.2e). Prisms above
 595 the reference are assigned a positive density contrast ($\Delta\rho = \rho_{below} - \rho_{above}$), and
 596 prisms below the surface a negative density contrast ($\Delta\rho = \rho_{above} - \rho_{below}$). All of
 597 these methods result in similar forward gravity calculations. See the Appendix ??
 598 for a comparison of these methods. Note that the absolute density option (Figure
 599 3.2b) has twice as many prisms as the other options, significantly increasing its
 600 computational expense, regardless of whether or not a buffer zone is used.

601 **Gravity edge effects**

602 Any forward gravity calculation of a surface will include gravitational edge effects.
 603 These effects are typically a decay in the gravitational field towards the edges of

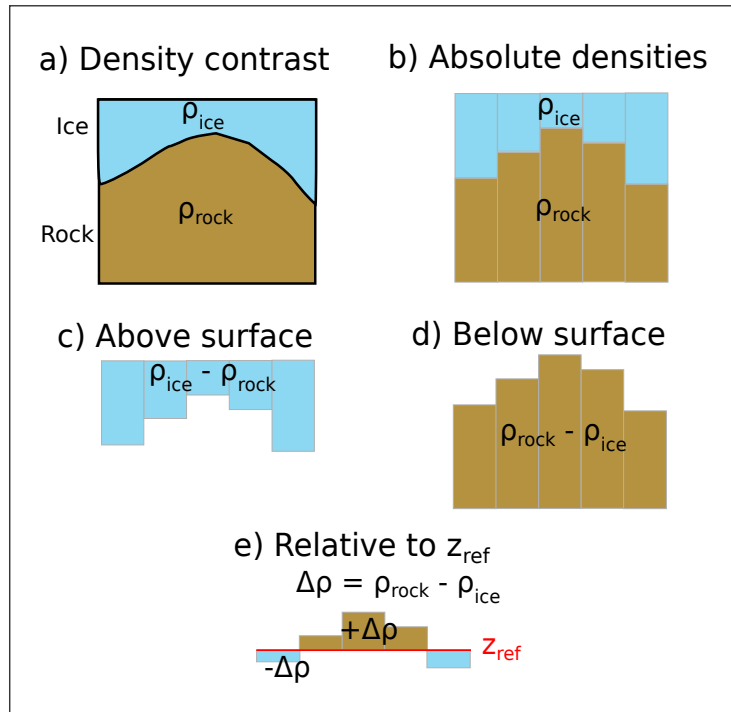


Figure 3.2: Equivalent methods of discretizing a density contrast (a) across a surface. b) Use absolute densities of the mediums above and below the reference, with prisms on either side. c-d) Use the density contrast across the surface, with prisms either above or below, and the sign of the density contrast reflecting whether they are above or below. e) Use a reference surface, with prisms above having a positive density contrast and prisms below a negative contrast.

the prism model due to the void space (density of 0) beyond the edge of the model. The magnitude of decay is dependent on the average thickness and density of prisms near the edge. Larger or denser prisms create a large contrast with the void space, resulting in a greater amount of decay. Therefore, the absolute density method of discretization (Figure 3.2b) produces the largest edge effects due to the high density values and large total thickness of the prisms. The relative density methods (Figure 3.2c-d) produce a smaller edge effect, since the prisms are only above or below the surface, reducing their total thickness. The density values are also less than in the absolute density method. The reference surface method (Figure 3.2e) produces the smallest edge effects due to both a) the mean prism thickness being smaller, and b) positive and negative density prisms having opposite edge effects, partially canceling each other out. This is only applicable if the reference level is located within the range of the values of the surface. Note that with a reference level completely above or below the surface, the reference method becomes identical to methods c) and d) of Figure 3.2.

619

A buffer zone can be used to reduce the impact of these edge effects by calculating forward gravity confined to an inner region, while the prism model extends beyond. This limits the majority of the edge effects to outside the region of calculation. Too large of a buffer zone will add an unnecessary amount of computation (more prisms), while too small of a zone will introduce unacceptably large edge effects to the calculations. The process of choosing the optimal buffer zone width is described in Appendix ??.

627 3.2.3 Isolating anomalies

628 For a successful geometric gravity inversion, the component of the observed gravity
 629 field resulting from the density contrast of interest must be isolated from all other
 630 gravity signals. This section describes the process of isolating the required anomaly.
 631 Since this section consists of synthetic gravity, discussion of correcting raw gravity
 632 measurements and deriving the various gravity anomalies are omitted. See Chapter
 633 4 for further discussion of gravity data processing. Here, *synthetic observed gravity* is
 634 taken to mean a complete Bouguer gravity disturbance, or topographically corrected
 635 gravity disturbance. This is defined as the gravity effect resulting from all anomalous
 636 density sources both inside and outside the ellipsoid (*Understanding the Bouguer*
 637 *Anomaly*, 2017). In other words, it represents all deviations between the real Earth
 638 and the reference earth model. Here, the topography-free gravity disturbance is
 639 taken to be the misfit, \vec{m} , in equation 3.1.

640 3.2.4 Regional vs. Residual gravity

641 The topography-free gravity disturbance is often simplified as consisting of two com-
 642 ponents, the regional and residual fields. The regional field typically dominates the
 643 signal, and is often the result of deeper and broader structures, such as Moho varia-
 644 tions. Superimposed on this signal is the residual field, which is typically the result
 645 of shallower structures. The terms residual and regional are relative; here, they are
 646 taken to mean the gravity effect of the bathymetry versus that of all deeper struc-
 647 tures, respectively. In this inversion, the residual, regional, and misfit are related
 648 by

$$\vec{m} = \vec{m}_{res} + \vec{m}_{reg}, \quad (3.10)$$

649 where \vec{m} is the overall data misfit, from equations 3.1. The residual misfit,
 650 \vec{m}_{res} , is the desired input into the inversion, and thus the regional component,
 651 \vec{m}_{reg} , must be removed prior to the inversion. This step proves to be one of the
 652 most challenging steps of a bathymetric inversion, especially in areas of limited
 653 constraints (Brisbourne et al., 2014). Removing an incorrect regional field, whether
 654 is its too much or too little, will directly impact the resulting bathymetry results.
 655 Regional-residual separation is also highly non-unique and benefits greatly from *a*
 656 *priori* constraints. Many methods of regional separation rely on the simplifying
 657 assumption that the regional field consist of longer-wavelength anomalies, while the
 658 residual field dominates the short wavelength components. Here, four methods of
 659 estimating the regional component of gravity are described.

- 660 1. Low-pass filter: With the assumption outlined above, a low-pass filter can be
 661 used to isolate the regional gravity. For this, a Gaussian wavelength filter is
 662 used and the filter width can be varied based on the expected regional anomaly
 663 wavelengths. This method requires the data to be gridded over the entire
 664 domain, which may be a problem for sparse surveys. or irregularly shaped
 665 domains. The choice of wavelength is subjective, and needs to be carefully
 666 considered. See Eisermann et al. (2020) for a bathymetry inversion utilizing
 667 this method of regional separation.
- 668 2. Trend removal: Similar to the low-pass filter method, a trend can be fit to the
 669 misfit data, representing the regional field. The order of the polynomial trend

is subjective and can be varied to suite the data. Again, this parameter choice requires care.

3. Equivalent source prediction: The equivalent sources technique is a method commonly used to grid, smooth, or upward-continue gravity data. It creates a set of point sources with densities, which when forward modelled, reproduce the measured gravity data. These sources are then used to predict the gravity anomaly at any desired point. The source depths can be varied to achieve the desired regional component. This technique is beneficial over low-pass filter and the trend removal in that it does not require the data to be gridded and can thus accommodate sparse surveys, or compilations of surveys at varying altitudes. It is computationally expensive compared to the above methods. Additionally, source depths are a subjective parameter, which need to be carefully chosen.
4. Constraint point minimization: The last method makes use of constraint points where the bathymetry depths are known. This inversion defines the residual component of misfit as the gravity effect from deviations of the true bathymetry with respect to the starting bathymetry. At constraints, there is no deviation between the starting and true bathymetries, and thus the residual component of the misfit should be zero at the constraints. This means the total misfit value at the constraints is equal to the regional component (equation 3.10). By sampling the misfit at each constraint, and fitting a surface to these values, a regional component is estimated. This technique has a few advantages. It imposes a form of smallness regularization, where the inversion won't significantly alter the depth of the constraint points, since the input residual at the points are ~ 0 mGal. Additionally, except for the gridding technique, this method doesn't require a subjective parameter, unlike the other methods. Similar to the low-pass filter and the trend removal, this method requires gridded data. If this data is sparse, or the constraints are not located near gravity observation points, some inaccuracies will be introduced. This technique has been used in several bathymetry inversions (An et al., 2019; Millan et al., 2020; Yang et al., 2021).

Other methods used to approximate the regional component include using high-altitude (satellite) gravity data (Muto et al., 2016; Tinto et al., 2015), the forward modelling of a geologic model, either inferred from 1) other geophysical data (Hodgson et al., 2019), 2) *a priori* geologic knowledge (Tinto & Bell, 2011), or 3) from an approximated crustal density distribution (Cochran et al., 2020; Tinto et al., 2019). Once estimated, the regional component is then removed from the total misfit, giving the residual misfit. This residual misfit ideally results solely from discrepancies between the starting and true bathymetries.

3.2.5 Running the inversion

Here, the necessary steps for running an inversion are explained. First, the Jacobian matrix is calculated (equation 3.8). Next, the matrix equation (equation 3.9) is solved, giving the necessary corrections to apply to the bathymetry. Additionally, this solutions needs to be constrained to account for the inherit non-uniqueness of the inversion. This is accomplished with various forms of regularization.

⁷¹⁵ **3.2.5.1 Jacobian matrix**

⁷¹⁶ The first step of the inversion is to calculate the sensitivity matrix, the Jacobian.
⁷¹⁷ Each entry of the Jacobian is the vertical derivative of gravity of a prism relative
⁷¹⁸ to a single observation point. Here two methods are derived for calculating these
⁷¹⁹ derivatives; 1) an annular approximation and 2) a finite differences approach.

⁷²⁰ **Annulus approximation**

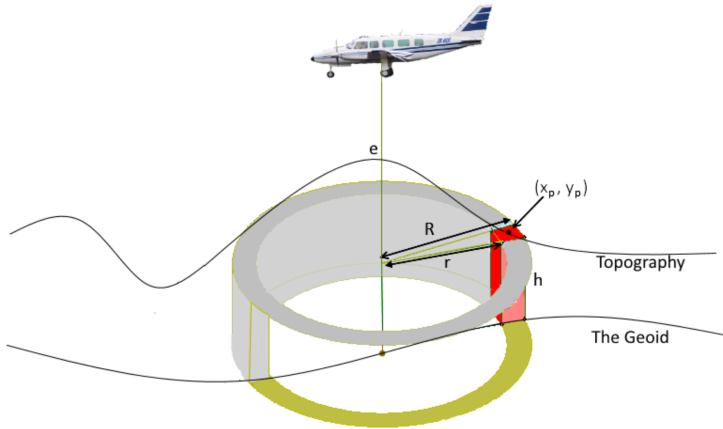


Figure 3.3: An illustration of an annulus of topography as an approximation for a vertical prism. From McCubbine (2016).

⁷²¹ A vertical prism can be approximated as a sector of an annulus (a cylindrical
⁷²² shell), as in Figure 3.3. This approximation greatly simplifies the calculation of the
⁷²³ vertical derivative of the prisms' gravity. The vertical component of gravity of an
⁷²⁴ entire annulus (grey hollow cylinder in Figure 3.3) is defined by

$$\delta g = 2\pi G\rho(R - r + \sqrt{r^2 + h^2} - \sqrt{R^2 + h^2}) \quad (3.11)$$

⁷²⁵ where ρ is the density, G is the gravitational constant, r and R are the inner and
⁷²⁶ outer radii, respectively, and h is the average height of the cylinder (Hammer, 1939).
⁷²⁷ r , R , and h are relative to the observation point, located in the center bottom of the
⁷²⁸ annulus. McCubbine (2016) provides an adaption of Equation 3.11 which isolates
⁷²⁹ the gravity of just a portion of this annulus (red section in Figure 3.3). This is
⁷³⁰ accomplished by adding an additional factor f , relating the area of the annulus to
⁷³¹ the area of a sector of it:

$$f = \frac{\alpha^2}{\pi(R^2 - r^2)} \quad (3.12)$$

⁷³² where

$$r = \sqrt{x^2 + y^2} - \sqrt{\frac{\alpha^2}{2}} \quad (3.13)$$

$$R = \sqrt{x^2 + y^2} + \sqrt{\frac{\alpha^2}{2}} \quad (3.14)$$

733 where α is the prism width, x , y , and z are coordinates of the prism center,
 734 relative to the observation point. This factor f is then multiplied by Equation 3.11
 735 to give the vertical component of gravity for a section of an annulus, $\delta g_{annulus} = f\delta g$.
 736 Taking the derivative of this with respect to h gives

$$\frac{\partial g}{\partial h} = 2f\pi G\rho h \left(\frac{1}{\sqrt{r^2 + h^2}} - \frac{1}{\sqrt{R^2 + h^2}} \right). \quad (3.15)$$

737 While the approximation of a prism as a section of an annulus introduces some
 738 errors, the calculation is efficient and simple to implement.

739 Finite differences approximation

740 Another option to calculate the vertical derivative for the Jacobian matrix is with
 741 numerical differentiation. For this, a small prism is added above each existing prism,
 742 its forward gravity is calculated and the result is divided by the small prism's height.
 743 This approximates the vertical derivative of gravity at the surface of the prism, rel-
 744 ative to the observation point.

745 Both methods adequately determine the Jacobian. The annulus method is a
 746 more simple calculation and is thus faster, but is likely less accurate and introduces
 747 singularities. These singularities occur if the prism is directly beneath the observa-
 748 tion point, so that either the inner or outer radii are negative (Figure 3.3). These
 749 singularities are resolved by shifting the observation point to a prism edge. Con-
 750 versely, the finite differences method, while it is a numerical approximation, uses
 751 analytical solutions for calculating the forward gravity (Fatiando a Terra Project
 752 et al., 2022; Nagy et al., 2000), and thus is valid in the entire domain, with no sin-
 753 gularities. This increased robustness makes the computation slower. Section 3.3.1
 754 compares the effectiveness and computation time of both of these methods.

756 3.2.5.2 Least-squares solver

757 With the Jacobian matrix and the vector of gravity residuals, equation 3.9 can be
 758 solved to find the set of surface correction values which minimize the fit function.
 759 Here, the matrix equation $\mathbb{J}\vec{x} = \vec{r}$ is solved with an iterative damped least squares
 760 algorithm (LSQR Paige & Saunders, 1982). LSQR accepts a damping parameter,
 761 which helps regularize the problem, preventing the solution from becoming too large.
 762 The choice of the damping value is important as it directly effects the inverted
 763 results. The optimal value can be chosen with a cross-validation routine following
 764 that of Uieda and Barbosa (2017), as described in below.

765 3.2.5.3 Regularization

766 Regularization is a series of techniques used to help constrain ill-posed inversion
 767 problems (Aster et al., 2018). Most potential field inversions, due to their inher-
 768 ent non-uniqueness, are ill-posed, containing many solutions which equally satisfy
 769 the data. Here regularization is split into *smallness* and *smoothness*. *Smallness*
 770 deals with adhering to *a priori* constraints, i.e. having the inverted surface eleva-
 771 tion match the previous bathymetry measurements (constraint points). *Smoothness*
 772 helps to achieve realistic topographic results, without major jumps or excessively
 773 steep slopes.

774 Smoothness

775 To achieve a form of smoothness regularization, damping is applied at each iteration
776 to the solver of the matrix equation. The damping should ensure a spatially smooth
777 result and help stabilize the inversion. One method to choose an optimal damping
778 value is a cross-validation of the input gravity data (Uieda & Barbosa, 2017). An
779 effective inversion should produce a topography which, when forward modeled, ac-
780 curately recreates observed gravity data which weren't included in the inversion.
781 This idea is the basis of the cross-validation routine. The observed gravity data is
782 split into two sets, a *training* and a *testing* set. For an individual damping value,
783 the inversion is run using only the training set. The final inverted bathymetry is
784 then forward modeled onto the observation points of the testing set. The difference
785 between the observed and forward gravity at these testing points is calculated. The
786 root mean square (RMS) of the differences provides a metric for the effectiveness
787 of the damping; this is referred to as the *score*. This process is then repeated for
788 a suite of damping values, and the value which produces the lowest score is used
789 as the optimal damping value. In this inversion, the gravity data, whether it is
790 airborne flight lines or scattered ground stations, is interpolated onto a regular grid
791 (See section 3.3.1). To create the testing set of observed gravity data, the original
792 data is interpolated onto a grid at half the desired grid spacing. This leaves the
793 training set with the desired amount of points. This grid spacing configuration is
794 shown in Figure 3.4.

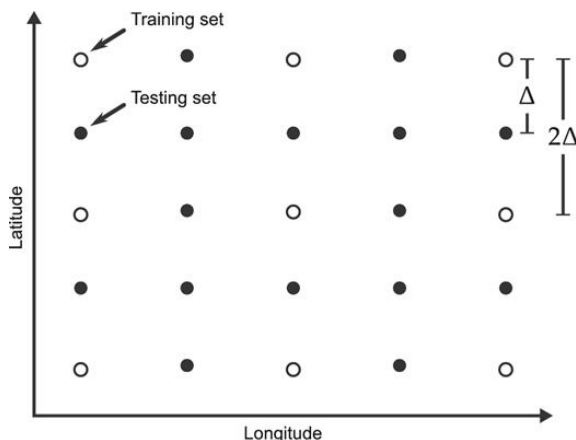


Figure 3.4: Configuration of observed gravity data observation points, split into training and testing sets. Reprinted from Uieda and Barbosa (2017).

795 Smallness

796 A form of smallness regularization is applied here to ensure the inversion results
797 adhere to any *a priori* bathymetry constraints. A portion of this smallness reg-
798 ularization is already accounted for when using the constraint point minimization
799 method of regional-residual separation. This method minimizes the residual compo-
800 nent of the gravity misfit at the constraint points by assigning the majority of the
801 misfit to the regional component. However, non-zero residual values near to the con-
802 straints will result in a non-zero correction of the prisms immediately surrounding
803 the constraint. For further smallness regularization, a weighting grid (Figure 3.5)
804 is used to ensure the surface correction values at each iteration are 0 at constraint
805 points. If only the prism immediately at the constraint point fixed, a *pedestal* effect

commonly develops. This is where the nearby prisms' surfaces freely move during the inversion, yet the constrained prism is fixed, resulting in either a pedestal or hole. To avoid this, the weighting grid smoothly decays from a value of 0 at the constraints, to a value of 1 at a distance. To create this grid, the minimum distance between each grid cell (prism) and the nearest constraint point is calculated. These values are then normalized from 0 to 1 (Figure 3.5). At each iteration, the least squares solver yields a grid of surface correction values. Before being added to the prism layer, the grid is multiplied by this weighting grid. This results in surface corrections of 0 for prisms located at constraint points, unmodified surface correction values far from constraint points, and a smooth taper between these two endmembers.

817

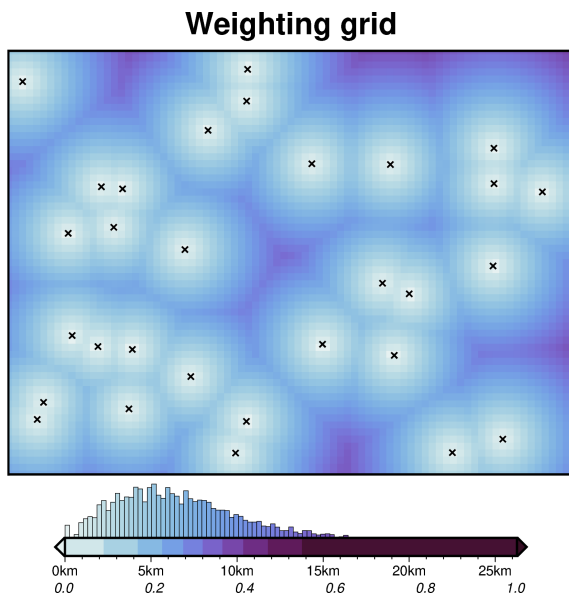


Figure 3.5: Weighting grid for the simple synthetic inversion, created from the minimum distance between each grid cell and the nearest constraint (black crosses). Grid values are normalized from 0 to 1 to produce the weighting grid (lower colormap annotations).

The above sections outline a single iteration of the inversion. Once the surface correction is calculated and the weights are applied, these values are added to startin bathymetry. This is then re-discretized into prisms. The updated prisms are then forward modelled to create a new predicted gravity, \vec{d}^{pred} . This is subtracted from the observed gravity, \vec{d}^{pred} , to get a new misfit, \vec{m} . Using the same original regional component, the updated residual gravity misfit, \vec{m}_{res} , is calculated. This is now the input into the second iteration of the inversion. This process is repeated until a user-determined termination. Next, we outline the four criteria for ending the inversion.

3.2.6 Stopping Criteria

The inversion is terminated on one of four stopping criteria:

- 829 1. when the inversion reaches a maximum number of iterations
- 830 2. when the ℓ^2 -norm of the residual ($\|\vec{r}\|_2$) is less than a set ℓ^2 -norm tolerance

- 831 3. if there is no significant variation in the ℓ^2 -norm between iterations (i.e. the
 832 $\Delta||\vec{r}||_2$ is less than a set tolerance)
- 833 4. if the ℓ^2 -norm increases above a certain threshold of the starting ℓ^2 -norm.

834 The maximum number of iterations is set as a safety margin to avoid excessively
 835 long running inversions. The ℓ^2 -norm tolerance is used to end the inversion before
 836 excessive over-fitting of noise in the data. This should be set to the square root of
 837 the assumed noise level of the gravity data. The $\Delta\ell^2$ -norm tolerance is used to end
 838 inversions which have reached their limit of reducing the ℓ^2 -norm. Finally, the upper
 839 limit of ℓ^2 -norm terminates run-away inversions.

840 **3.2.7 Software implementation**

841 The inversion algorithm described here is implemented within the Python program-
 842 ming language. The algorithm uses many open-source scientific libraries. These in-
 843 clude Harmonica for the forward gravity modelling of prisms and equivalent sources
 844 calculations (Project et al., 2023; Soler & Uieda, 2021), Verde for various spa-
 845 tial operations (Uieda, 2018), PyGMT and Antarctic-Plots for figure creation (M.
 846 Tankersley, 2023; Uieda et al., 2021), Scipy for least squares regression (Virtanen
 847 et al., 2020), and Optuna for hyperparameter optimization (Akiba et al., 2019).
 848 The majority of the experiments were run in Jupyter notebooks (Pérez & Granger,
 849 2007), which are documented to explain the details of using the software. All source
 850 code, results, and figures involved in this chapter are made available in an online
 851 GitHub repository (???). See Appendix B.3 for the hardware used in this study and
 852 a summary of the computation times for various processes.

853 **3.3 Synthetic models**

854 To assess the performance of the inversion and showcase its use, it is applied to
 855 a suite of synthetic test models. Each model has three components; 1) the ‘true’
 856 bathymetry surface, which the inversion is expected to model, 2) the ‘observed’
 857 gravity data and 3) the ‘starting’ bathymetry model, which is a low resolution
 858 version of the true surface. The only inputs into the inversions are the observed
 859 gravity data and the starting bathymetry. The true bathymetry is only used to
 860 evaluate the performance of each inversion. The observed gravity data contains the
 861 forward gravity calculated from the true bathymetry, plus, in some cases, additional
 862 noise and other gravity signals such as a regional field. The starting bathymetry
 863 is created by sampling the true bathymetry at a set of points. These values are
 864 then used to re-grid the data for the entire region using a bi-harmonic spline gridded
 865 (Uieda, 2018). This simulates the bathymetric knowledge of many ice shelves, where
 866 we have sparse direct measurements of bathymetry, such as drill holes, or single-point
 867 seismic surveys. These points are referred to as the constraints. The first set of
 868 models (Section 3.3.1) sets a baseline performance expectation of the inversion, with
 869 no noise, dense gravity observation points, and no additional components included
 870 in the observed gravity. For this model the synthetic bathymetry is created with
 871 Gaussian functions of various amplitudes and wavelengths. With this same simple
 872 model, the observed gravity data is re-gridded at a lower resolution and random
 873 noise is added, to better simulate a gravity survey. Next, a ‘regional’ component

of the gravity field is added to the observed data (Section 3.4). Finally, a new synthetic model is introduced, which is created from real bathymetry data from Antarctica's Ross Sea (Section 3.5). This model tests the inversion's capabilities with more realistic bathymetric features expected for sub-ice shelf environments.

3.3.1 Simple model

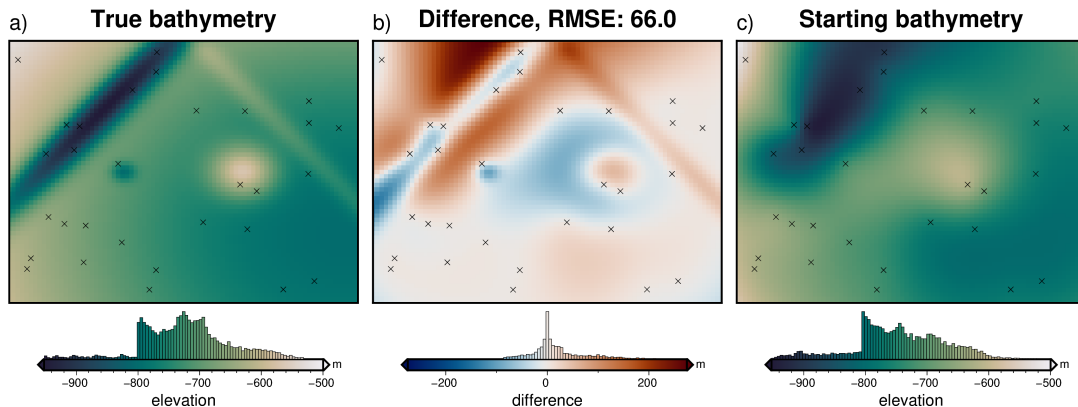


Figure 3.6: Simple synthetic model bathymetry. **a)** True bathymetry created from Gaussian functions, **b)** difference between a and c, and **c)** starting bathymetry, created from the sampling and re-gridding of the true bathymetry at 30 points (black crosses).

Model setup

Simulating typical sub-ice shelf bathymetry, this model (Figure 3.6a) has an average elevation of ~ -700 m and ranges between ~ -400 m and ~ -1000 m. It contains features of various wavelengths, amplitudes, and shapes; namely two circular features and two linear features. Overall, the grid is eastward deepening and contains a shallow and wide E-W trough through the center. The model domain is 80 km x 60 km, with 1 km grid cells (4800 cells). A 6 km buffer zone in all directions was included to limit gravitational edge effects. 30 randomly located constraint points were used to create the starting bathymetry (Figure 3.6c). The starting bathymetry has an RMS difference with the true bathymetry of 66 m.

To forward model the gravity of the true bathymetry, a layer of adjacent vertical right-rectangular prisms was created using the reference discretization method (Figure 3.2e) with the mean elevation as the reference level. A density contrast of $\Delta\rho = 1276 \text{ kg m}^{-3}$ (contrast between seawater (1024 kg m^{-3}) and sediment (2300 kg m^{-3})), was used, with $+\Delta\rho$ for prisms above the reference, and $-\Delta\rho$ for prisms below the reference. The forward gravity of this prism layer was calculated at a constant height of 1000 m (roughly 1700 m above the bathymetry) on a regular grid at half the grid spacing (500 m) of the bathymetry. This represents the observed gravity data (Figure 3.7a) and consists of both the training and testing data sets used for the cross-validation (Section 3.2.5.3, Figure 3.4).

The low resolution starting layer was discretized in the same method, and the same density contrast was used. The forward gravity of these starting layer prisms results in the predicted gravity (Figure 3.7c). To account for any offset between the observed and predicted data, the observed data is DC shifted to minimize the

905 differences at the constraint points. The difference between the shifted observed and
 906 the predicted data gives the gravity misfit (Figure 3.7b). Since there is no regional
 907 component in this synthetic model, the input into the inversion, the residual misfit,
 908 is equal to this total misfit (equation 3.10). This residual misfit describes the ability
 909 of the starting model to predict the observed data.

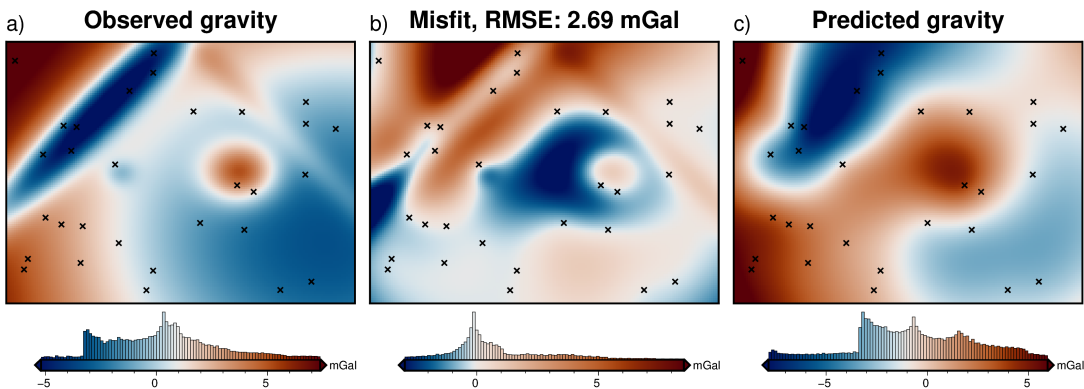


Figure 3.7: a) Synthetic gravity data generated from the true bathymetry, b) the residual anomaly, defined as the difference between a and c, and c) the predicted gravity from the starting bathymetry (Figure 3.6c).

910 Cross validation

911 To find the optimal value for the regularization damping parameter, the cross-
 912 validation method of Uieda and Barbosa (2017) is used (Section 3.2.5.3). The full
 913 set of observed data with a 500 m spacing ($N = 19481$), was separated into the
 914 training ($N = 4941$) and testing set ($N = 14540$). With the grid configuration from
 915 Figure 3.4, the resulting training data was on a regular 1 km grid, which matches
 916 the grid of the bathymetry. This training data set was used as the input to 10
 917 inversions. Each inversion used a different damping value between 10^{-4} and 10^{-1} .
 918 The resulting inverted bathymetry of each inversion was then forward modelled on
 919 the observation points of the testing data set (not used in the inversion). The RMS
 920 difference between the forward modelled gravity value and the initial residual misfit
 921 values was calculated, giving the cross-validation score (Figure 3.9a). Of the 10
 922 inverted bathymetry models, the model with the lowest score is retained.

923 This model is shown in Figure 3.8c, and resulted from a damping value of 10^{-2} .³³ This
 924 inverted bathymetry has a RMS difference with the the true bathymetry of 8
 925 m, and a RMS difference at the constraint points of 1 m. Figure 3.9b shows a profile
 926 across the model. The overlap of the true (red) and inverted (blue) bathymetry in the
 927 first panel show the effectiveness of the inversion at recovering the true bathymetry.
 928 The lower panel show the inversion's ability to minimize the misfit between the
 929 observed gravity (red) and the forward response of the inverted bathymetry (blue).
 930 The inversion was able to recover all the features of the true bathymetry, with only
 931 minor errors along the edges of the domain, and adjacent to constraint points. For
 932 this simple model, the inversion converged in 28 iterations, with a total computation
 933 time of 24 seconds and a final RMS residual misfit of 0.021 mGal. It terminated due
 934 to the ℓ^2 -norm decreasing between the set threshold of 0.15 (0.0225 mGal).

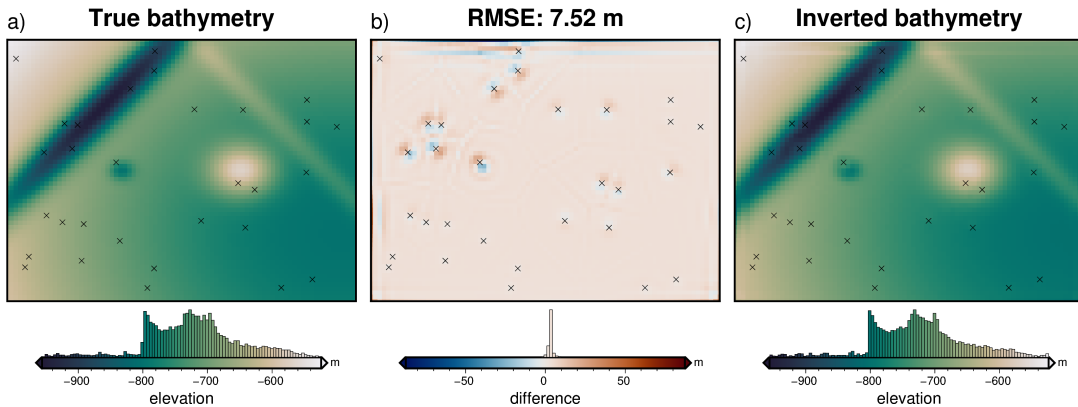


Figure 3.8: Inverted results with optimized parameters, using the annulus approximation method of calculating the Jacobian matrix. **a)** True bathymetry, **b)** difference between a and c, and **c)** final inverted bathymetry. Black crosses are constraint points. The RMS difference with the true bathymetry at these constraints is 1 m

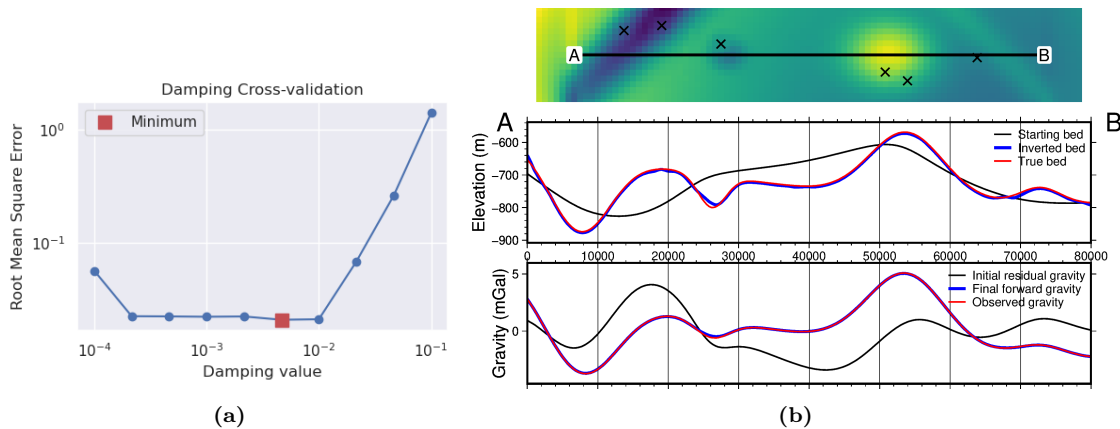


Figure 3.9: Cross-validation and profiles for the simple synthetic inversion. **a)** Cross-validation curve showing the optimal damping parameter (red square). Both axes are on a logarithmic scale. **b)** 2D profile of the inversion results. The top panel shows profile location and constraint points (black crosses). The middle panel contains topographic profiles of the starting, inverted, and true bathymetries. The bottom panel contains gravity anomaly profiles.

935 Comparing vertical derivative methods

936 Section 3.2.5.1 presented two methods for calculating the vertical derivative of gravity
 937 of a prism. This vertical derivative is used to create the Jacobian matrix (equation
 938 3.9) and needs to be calculated at each iteration of the inversion. The above
 939 cross-validation and inversion were performed using the *annulus approximation* of
 940 the vertical derivative. Here, this process is repeated with the *finite differences*
 941 method of the vertical derivative. Figure 3.10) shows the results of this inversion.
 942 The optimal damping parameter was 10^{-2} , and the inversion resulted in a RMS
 943 difference with the true bathymetry of 9 m, compared to 8 m for the annulus ap-
 944 proximation. Figure 3.11 shows the inversion convergence curves for the inversion of
 945 the annulus approximation and the finite differences methods. The inversion with
 946 the annulus approximation was $\sim 600\%$ faster to converge than the finite differences
 947 method (24 sec vs 177 sec). Because these vertical derivatives need to be recalculated
 948 at each iteration, a large portion of the inversion time is spent performing these
 949 calculations. This comparison shows the annulus approximation is not only signifi-
 950 cantly faster, but results in comparable, or slightly more accurate, inversion result.

951 For the remainder of this chapter, only the annulus approximation will be used.

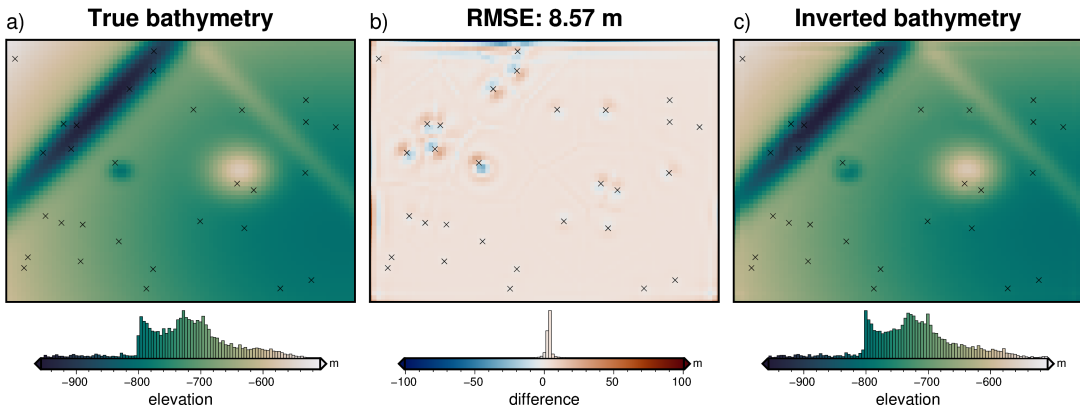


Figure 3.10: Inversion results with optimized parameters using the finite differences method. **a)** True bathymetry, **b)** difference between a and c, and **c)** final inverted bathymetry. Black crosses are constraint points. The RMS difference with the true bathymetry at these constraints is 2 m

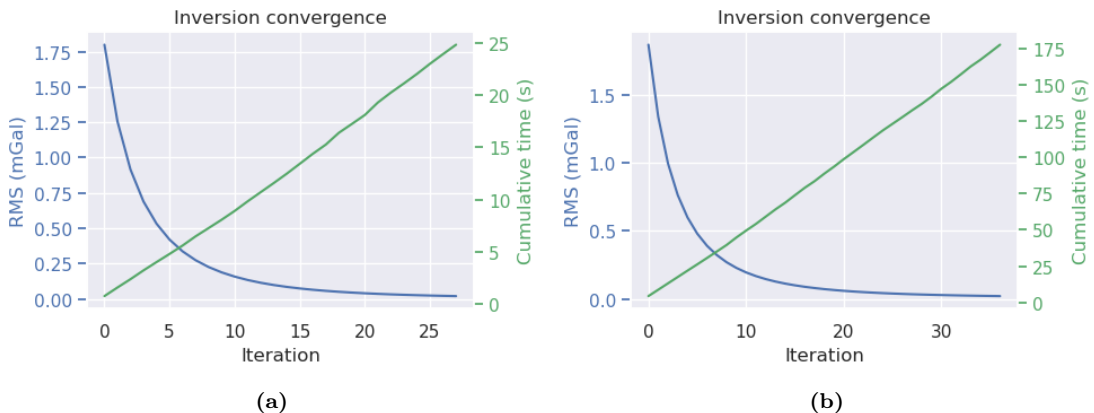


Figure 3.11: Inversion convergence curves for the two method of creating the Jacobian matrix. Blue line (left y-axis) shows the RMS of the residual misfit at each iteration of the inversion. Green line (right y-axis) shows the cumulative time to complete the inversion. **a)** Results for the annulus approximation method of finding the vertical derivative. **b)** Results for the finite differences method.

952 Added noise

953 To test the effect of noise in the gravity data, which is inevitable in data collection,
 954 especially so in airborne surveying, the observed gravity was contaminated with
 955 noise. The noise was from a Gaussian distribution with a mean of 0 mGal and
 956 a standard deviation of 2% of the max absolute value of the data ($\sim .16$ mGal).
 957 Similarly, Rashidifard et al. (2021) used 5% noise in their synthetic gravity inversion
 958 while Uieda and Barbosa (2017) use 5 mGal of noise, which for their synthetic
 959 application equated to $\sim 1\%$ of the max absolute value. Using this noise-corrupted
 960 gravity data, the same damping parameter cross validation was run as previously
 961 (Figure 3.13a) and the lowest score was achieved with a damping value of 10^{-2} . Figure
 962 3.12 shows the inversion results of this noise-contaminated model. The inversion
 963 converged in 18 iterations, with a total computation time of 18 seconds and a final
 964 RMS residual misfit of 0.16 mGal. It terminated after the ℓ^2 -norm became lower
 965 than the set tolerance of 0.4 (0.16 mGal). This tolerance was set to match the known

level of noise. The inverted bathymetry had a RMS difference of 12 m with the true bathymetry, and a RMS difference of < 1 m at the constraint points. Figure 3.13b shows the inversion is still able to reproduce the observed gravity (lower panel), but a component of the noise was introduced into the final bathymetry (upper panel). All major features of the true bathymetry are recovered, albeit not as accurately as the no-noise model (Figure 3.8).

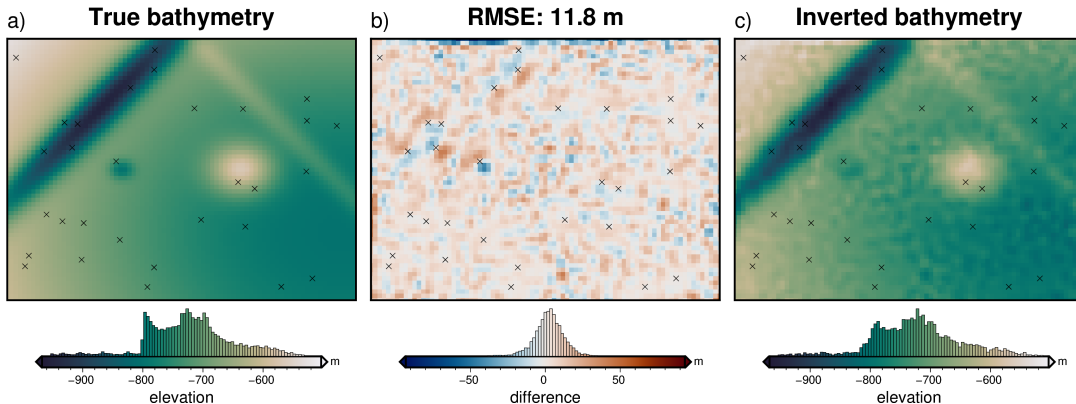


Figure 3.12: Simple synthetic model inversion results with 2% added noise (0.16 mGal). **a)** True bathymetry, **b)** difference between a and c, **c)** final inverted bathymetry. Black crosses are constraint points. The RMS difference with the true bathymetry at these constraints is < 1 m.

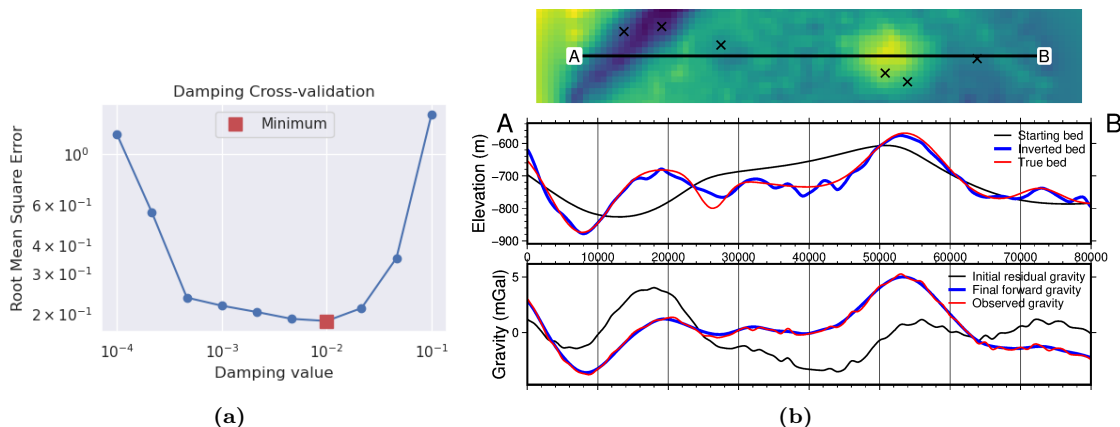


Figure 3.13: Cross-validation and profiles for the inversion with noise. **a)** Cross-validation curve showing the optimal damping parameter (red square). **b)** 2D profile of the inversion results. The top panel shows profile location and constraint points (black crosses). The middle panel contains topographic profiles of the starting, inverted, and true bathymetries. The bottom panel contains gravity anomaly profiles.

972 Down-sampled data

The previous two models used observed gravity data collected on a grid of observation points at the same grid spacing as the prism layer (1 km). This represents a very dense gravity survey. Gravity surveys are often relatively sparse compared to the resolution of the surface they are attempting to recover in an inversion. This section tests the effect of changing the resolution of the gravity data, to simulate a coarser gravity survey. Simply sampling the gravity data at a coarser resolution leads to a checker-boarding effect, where the inversion alters prisms nearby the gravity observations, but not prisms further away. For this reason, it is recommended

here to re-grid the observed gravity data at a similar grid spacing to the prism layer. This can be accomplished with standard gridding techniques, such as minimum curvature or bi-harmonic splines (see section 3.4.2). However these techniques aren't well suited for potential field data since they don't account for the variation in observation heights (Soler & Uieda, 2021). An alternative method of interpolating the gravity data onto a finer resolution grid is the equivalent sources technique (Dampney, 1969)¹.

988

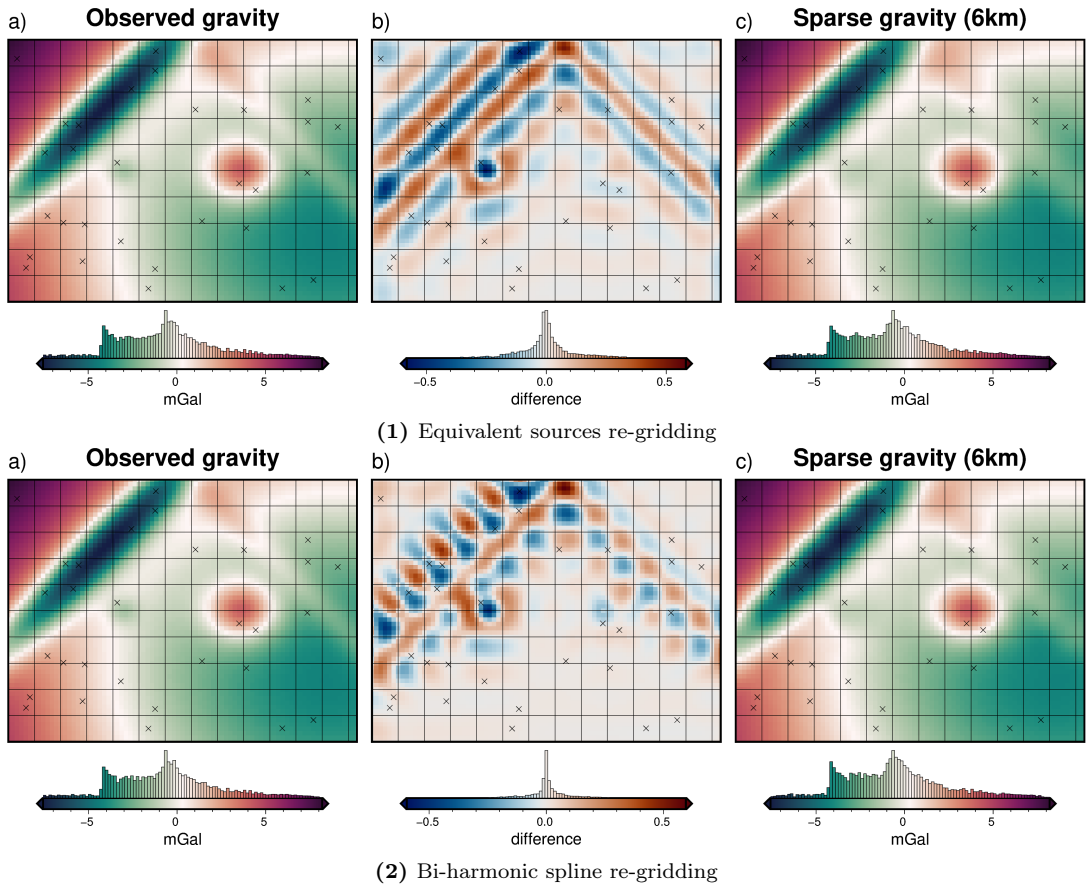


Figure 3.14: Creating a low-resolution observed gravity survey. **Top panel** shows results using the equivalent source technique of gridding gravity data. **Bottom panel** shows simple gridding using a bi-harmonic spline. **a)** Original observed data on a 1 km grid, **b)** gravity signal lost due to sampling and re-gridding, **c)** the low-resolution observed gravity (6 km spacing) re-gridded at 1 km with either equivalent sources (top) or a regular gridding algorithm (bottom). Black crosses show constraint points and black lines show 6 km grid.

Here, the original gravity data, on a 1 km grid, is sampled at a 6 km spaced grid to represent a low resolution survey with observations every 6 km. A series of point sources are created at depth, and their densities are altered to best reproduce the observed gravity data. Once this process of fitting the source parameters to the data is accomplished, the gravity field can be predicted anywhere. For this application, the equivalent sources are predicted onto an even 1 km grid, to match the spacing of the bathymetry. Figure 3.14 shows the results of this process (top panel) and the results using a simple gridding without equivalent sources (bottom panel). Subplots a) shows the original observed gravity data (just training points) on

¹The equivalent sources technique is also used in this study as a means of regional separation (see section 3.2.4, this is a similar application but for different purposes).

a 1 km grid. This grid is sampled onto a 6 km grid (black grid lines), and re-gridded at 1 km (subplots c). Subplots b) shows the difference, which represents the lost data resulting from the sparse survey. Typically the equivalent sources gridding technique is most beneficial to account for variations in observation heights. Here, even with constant elevations, there are noticeable differences between equivalent source gridding and simple gridding with bi-harmonic splines.

The equivalent-source resampled grid is used, with no added noise, in the same inversion procedure as the previous sections. The cross validation (Figure 3.16a) resulted in an optimal damping value of 10^{-3} . The inverted bathymetry with this damping value is shown in Figure 3.15. The inversion was completed in 54 seconds and 31 iterations with a final RMS residual misfit of 0.018 mGal. The inversion was terminated due to the ℓ^2 -norm decreasing below the set threshold of $0.15 \text{ mGal}^{1/2}$. The inverted bathymetry had a RMS difference of 9 m with the true bathymetry, and a RMS difference of 1 m at the constraint points. While the overall difference from the true bathymetry is low, this inversion failed to fully recover the small circular depression. Figure 3.14 shows that the nearest observation point (intersection of gridlines) was on either side of this anomaly, and thus the sparse gravity survey used here failed to image the true magnitude of the feature. Figure 3.16b shows the absence of this feature in the inverted bathymetry.

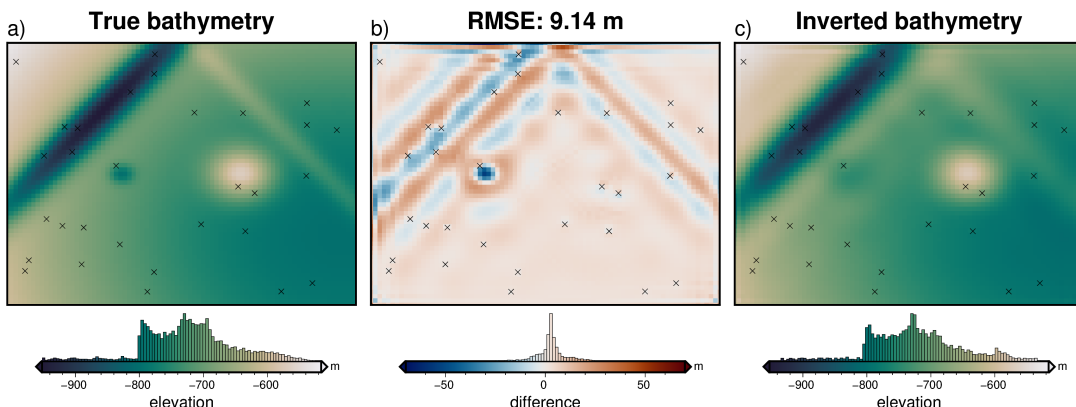


Figure 3.15: Simple synthetic model inversion results with input data resampled at 6x the bathymetry grid spacing (6 km). **a)** True bathymetry, **b)** difference between a and c), and **c)** final inverted bathymetry. Black cross show constraint points. The RMS difference with the true bathymetry at these constraints is 1 m.

3.3.2 Ensemble of Noise and Sampling values

To test the relative importance's of the level of noise and the resolution of the gravity data (i.e. station/flight line spacing), an ensemble of 100 inversions were run, with 10 noise levels between 0 and 9%, and 10 gravity resolutions between 1 and 10 km. The noise level percentages are of the maximum absolute value of the data, equating to 10 levels between 0 and 0.74 mGal. The differing gravity resolutions were created with the sampling and re-gridding of equivalent sources outlined in the above section. For each set of noise and spacing values, the cross validation routine was used to find the optimal damping parameters and associated inverted bathymetries. Each of these 100 inversions were then compared to the true bathymetry yielding a RMS difference for each.

Figure 3.17 shows the results of this ensemble of inversion. Each grid cell represents a single inversion, with the level of noise and gravity resolution for the

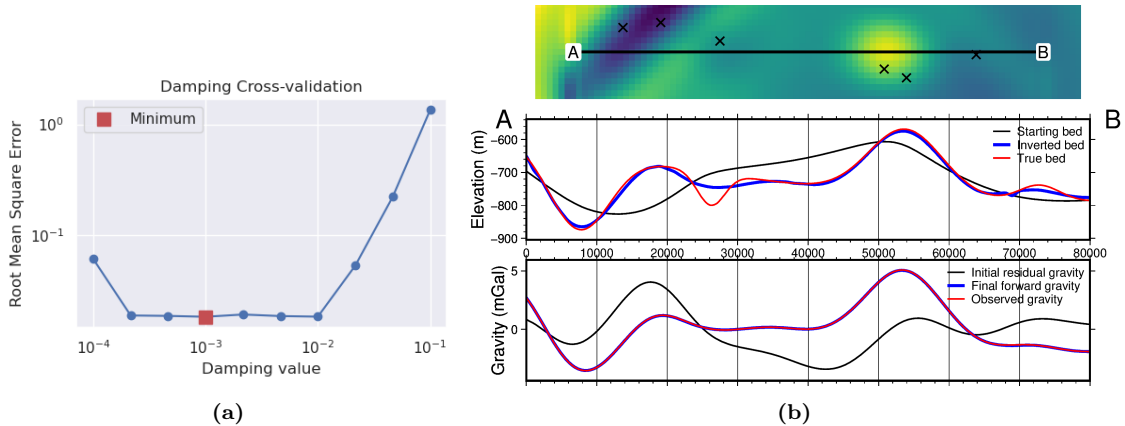


Figure 3.16: Cross-validation and profiles for the 6 km resampled inversion. **a)** Cross-validation curve showing the optimal damping parameter. **b)** 2D profile of the inversion results. The top panel shows profile location and constraint points (black crosses). The middle panel contains topographic profiles of the starting, inverted, and true bathymetries. The bottom panel contains gravity anomaly profiles.

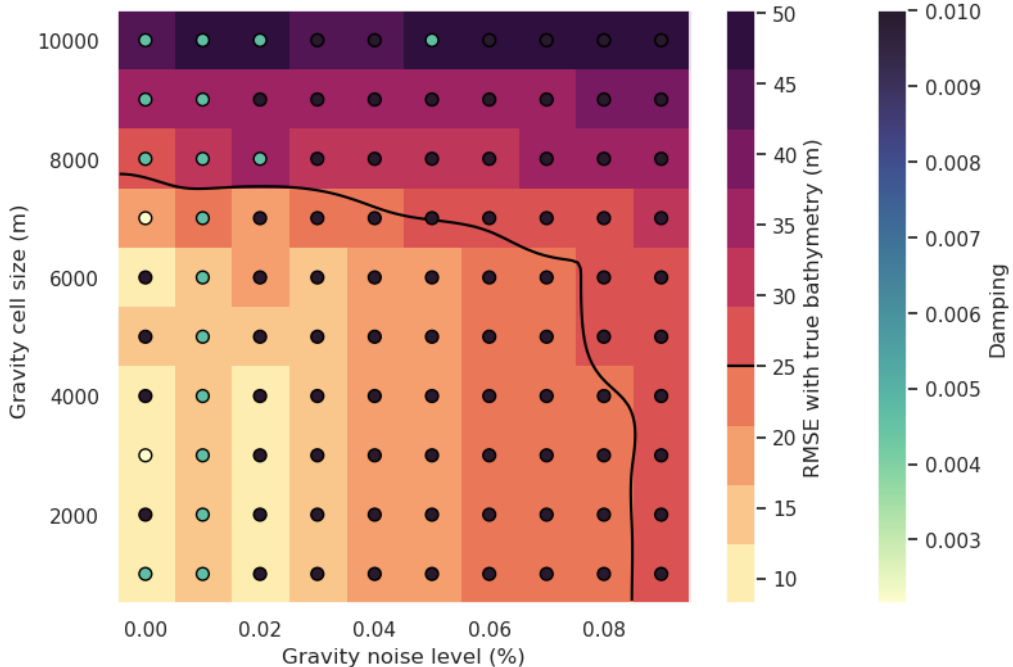


Figure 3.17: Ensemble of noise levels and gravity spacing for the simple synthetic model. Grid cell color indicates each inversion's RMS difference with the true bathymetry. Circles' color indicate the optimal damping value found for each inversion's cross validation. Black line shows the 25 m RMSE contour, indicative of the amplitude of the smallest amplitude features.

inversion indicated by the x and y axis, respectively. The background color (warm colors) indicates each inversion's resulting RMS difference with the true bathymetry. Colored circles show the optimal damping value for each inversion found through the cross-validation. This shows a general decrease in the inversion's accuracy with either more noise, or low-resolution gravity data. The smallest bathymetric features which this inversion ideally should recover have amplitudes of tens of meters (small circular depression and narrow ridge). The RMSE here indicates a baselevel of error in the inversions, while the error in the vicinity of the short wavelength bathymetry features is likely higher (Figure 3.15b). Inversions with RMSE's of 10's of meters

will likely fail to resolve these small features. For this inversion, an RMSE of 25 m (black contour in Figure 3.17) approximately equates to a gravity observation spacing greater than 8 times the prism layer spacing, and a noise level higher than 8% of the survey's max absolute value.

3.4 Adding a regional component

Now that the inversion has been demonstrated to adequately recover bathymetry with various levels of noise and resolutions of the input gravity data, an additional complexity is added. This complexity is a regional component of the observed gravity field. To account for this, the inversion remains the same, but the regional component of the gravity misfit must be removed beforehand (equation 3.10). In this section, first the four methods of regional separation laid out in 4.2.2 are compared. Next, one of these methods, constraint point minimization, is further investigated. Lastly, the effects of noise and gravity survey spacing are explored.

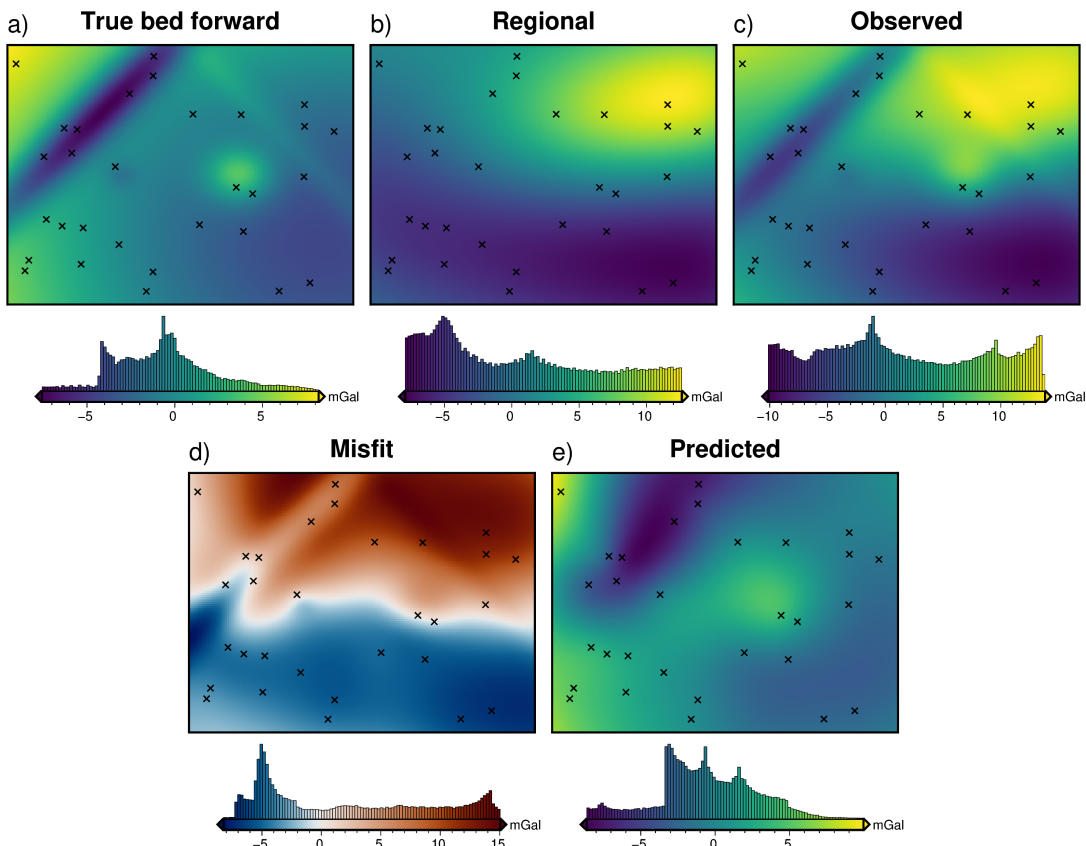


Figure 3.18: Gravity components and anomalies for the simple synthetic model with the addition of a regional field. **a)** the forward gravity of the true bathymetry, **b)** the regional component of gravity, **c)** the observed gravity from the combination of a and b, **d)** the gravity misfit from the difference between c and e, and **e)** the predicted gravity from the forward calculation of the starting bathymetry.

This model uses the same starting bathymetry (Figure 3.6) as the previous section, but the observed gravity includes a regional field, which represents the portion of observed gravity signal resulting from unknown crustal sources, such as anomalous bodies or crustal thickness variations. This component (Figure 3.18b) is calculated from a synthetic topography with a median elevation of -4300 m and a density con-

1057 trast of 700 kg m^{-1} . Its range of gravity values is set to be the dominant signal in the
 1058 observed gravity, but not large enough to fully mask the signal of the bathymetry
 1059 signal. Figure 3.18 shows the various components of the gravity and resulting misfit
 1060 for this model.

1061 3.4.1 Regional separation methods

1062 The four methods of regional separation discussed in section 3.2.4 each have at least
 1063 one hyper-parameter which affects their calculation of the regional field. For each
 1064 method these include

- 1065 1. Low-pass filter: the distance width of the Gaussian filter.
- 1066 2. Trend removal: the degree of the polynomial trend fit to the misfit.
- 1067 3. Equivalent source prediction: the depth and damping parameters of fitting
 1068 sources to the data (Soler & Uieda, 2021).
- 1069 4. Constraint point minimization: parameters for the associated gridding method,
 1070 such as the tension factor for minimum curvature gridding (W. H. F. Smith
 1071 & Wessel, 1990) or the minimum distance and damping parameter for bi-
 1072 harmonic spline gridding (Uieda, 2018).

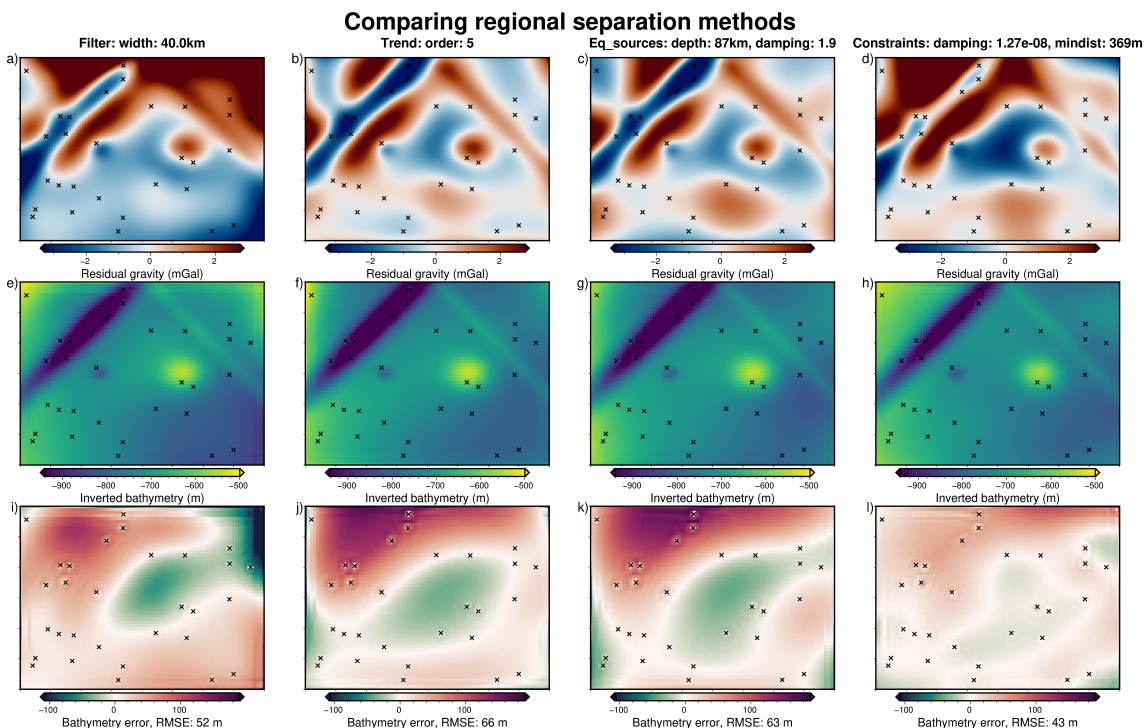


Figure 3.19: Comparison of inversion with 4 regional separation methods. First row (a-d) shows residual gravity misfit after regional separation. Second row (e-h) shows the inverted bathymetry for each method. Third row (i-l) shows the error of the inverted bathymetries with the true bathymetry. Constraint points shown as black crosses. Colormaps are identical for each row

1073 Since for this synthetic model the true regional field is known (Figure 3.18b),
 1074 the effect of the parameters associated with each of the four methods can be ex-
 1075 plored. Excluding the constraint point minimization method, an optimization is run
 1076 for each method, with the goal of finding the parameter values which minimizes the

1077 RMS difference between the true and calculated regional gravity. Each optimization
1078 has 20 trials. The constraint point minimization doesn't require an optimization
1079 because the various gridding parameters won't significantly effect the RMS difference
1080 between the resulting regional field and the true field. However, the gridding
1081 parameters will effect the inversion itself; this is explored in the next section. For
1082 this comparison of the regional removal method, the constraint point minimization
1083 method uses bi-harmonic spline gridding and the gridding parameters (minimum
1084 distance and damping) are chosen with a cross-validation (Uieda, 2018). The best
1085 regional field (lowest RMS with the true regional field) of each method was found
1086 with the following parameters:

- 1087 1. a 40 km filter width for the low pass filter method
- 1088 2. a 5th order trend for the trend removal method
- 1089 3. source depth of 87 km and a damping value of 1.9 for the equivalent source
1090 technique
- 1091 4. a gridded damping of 1.27×10^{-8} and a minimum force point distance of 369 m
1092 for the bi-harmonic spline gridded of the constraint point minimization method.

1093 Each of these regional fields were then removed from the gravity misfit, producing
1094 the residual anomalies (Figure 3.19a-d). These resulting residuals were then input
1095 into an inversion, resulting in the inverted bathymetries of d-h of Figure 3.19, and
1096 the bathymetry error relative to the true bathymetry was found (Figure 3.19i-l). For
1097 these inversions a constant damping value of 10^{-2} was used. This comparison of
1098 regional separation methods shows that the constraint point minimization method
1099 (Figure 3.19l) produces the best inverted bathymetry, both visually (Figure 3.19h),
1100 and based on the RMS difference with the true bathymetry (43 m). The remainder of
1101 this section further examines the constraint point minimization method of regional
1102 separation.

1103 3.4.2 Constraint point minimization

1104 The constraint point minimization method assumes that at locations of known
1105 bathymetry there is no residual component of gravity misfit, and the regional com-
1106 ponent entirely equals the misfit. To implement this, misfit values at the constraints
1107 are sampled and used to create a region-wide grid of regional values. This grid is
1108 then removed from the misfit to get the residual misfit (equation 3.10). This grid-
1109 ding can be accomplished by many techniques, which at an initial inspection appear
1110 to produce similar results. Here, two methods of gridding and their gridding param-
1111 eters are compared, and the impact on the inverted bathymetry are shown. These
1112 gridding methods are tensioned minimum curvature (W. H. F. Smith & Wessel,
1113 1990) and bi-harmonic splines (Sandwell, 1987).

1114 Tensioned minimum curvature

1115 Tensioned minimum curvature gridding is a commonly used technique for gridding
1116 sparse data which fits the smoothest possible surface while still matching the data
1117 (Wessel & Bercovici, 1998). It allows variation in the location of maximum cur-
1118 vature through the tension factor parameter. A tension factor of 0 results in the
1119 minimum curvature solution (maxima and minima allowed anywhere), while a value

of 1 localizes the curvature at the data points (maxima or minima only allowed at the data points) (W. H. F. Smith & Wessel, 1990). A tension of 0.25 is suggest for potential fields data (Wessel et al., 2019). Tensioned minimum curvature has been used in several bathymetric inversions for constraint point minimization (An et al., 2019; Millan et al., 2020; Yang et al., 2021).

Bi-harmonic splines

The second method of gridding the sampled gravity misfit values uses bi-harmonic splines. This method uses Green's functions and a least squares fit to the data (Sandwell, 1987). Computation time for this technique is approximately proportional to the cube of the number of data, making it computationally expensive for large datasets (Deng & Tang, 2011). There are two parameters which can be adjusted; the minimum distance from the point forces to the data (*mindists*) and a damping regularization factor (*damping*). As implemented in the *SplineCV* class of the Python package Verde (Uieda, 2018), an automated cross-validation of the data can be used to identify the values of *mindists* and *damping* which are able to best predict the data. Once the parameters are determined, and the data is interpolated, the interpolation can be predicted at any location, such as on the nodes of a uniform grid.

Despite it's slow run time with large datasets, bi-harmonic spline gridding has several advantages over tensioned minimum curvature gridding. It allows the incorporation of data uncertainties into the fitting via a weighting parameter. With the use of cross-validation, there are no subjective parameters which can significantly alter the results. Lastly, the predicted data don't need to be on a regular grid, which is useful for irregularly shaped domains which don't adhere to a rectangular region. In their bathymetry inversion, Millan et al. (2020) point out features in their inverted bathymetry which likely result from the minimum curvature gridding technique. Apart from this, there appears to be little work related the how the gridding procedure effects this aspect of a bathymetry inversion.

Gridding comparison

In this section the effect which the gridding process has on the inverted bathymetry is analyzed. Four sets of regional separations were conducted, three using the tensioned minimum curvature technique, and one using the bi-harmonic spline technique. For the three minimum curvature separations, the tension factors used were the end members, 0 and 1, and the suggested value for geopotential data, 0.25. For the bi-harmonic spline, a cross-validation with 20 values each (400 sets) of parameters *mindists* and *damping* was conducted, and the parameter sets producing the best score was used. For each of the four calculated regional fields, the resulting residual fields (Figure 3.20a-d) were used as inputs to an inversion. All four inversion had the same damping parameter of $10^{-2.6}$. The difference between the resulting inverted bathymetry and the true bathymetry of each model is shown in Figure 3.20i-l. To help visualize the difference in the resulting residual grids, 3.20e-h show the vertical derivative of the residual fields. This highlights that while the residual values at the constraints are all similar, the slope of the residual in the vicinity of the grids is

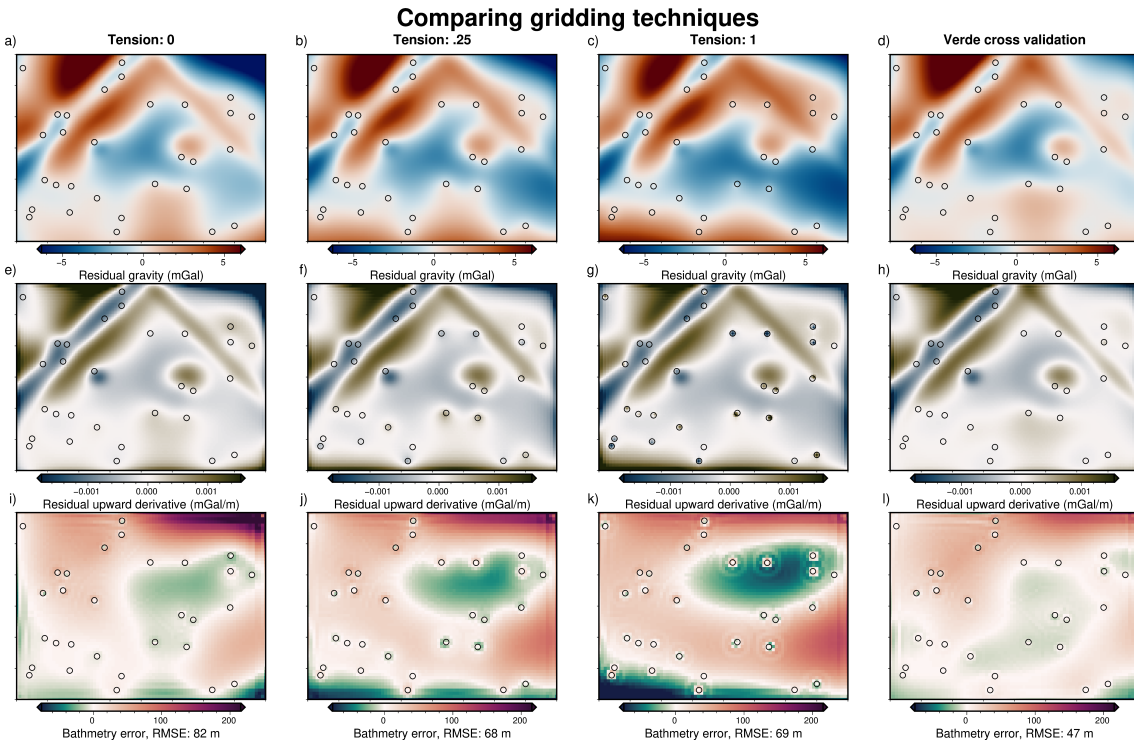


Figure 3.20: Comparison of gridding techniques for the constraint point minimization method of regional-residual separation. By sampling the misfit at constraints, and re-gridding over the entire domain, the regional component of the misfit is estimated. Gridding methods include minimum curvature gridding with tension factors of 0 (**column 1**), 0.25 (**column 2**), 1 (**column 3**), and cross-validated bi-harmonic spline gridding (**column 4**). Resulting gridded regional components were removed from the misfit grids to produce the residual grids (**a-d**). Second row (**e-h**) shows the vertical derivative of the residual, to highlight the gridding variations. Third row (**i-l**) shows the error of the inverted bathymetries with the true bathymetry. Constraint points shown as open circles. Colormaps are identical across all columns.

strongly dependent on the gridding method². Additionally, the minimum curvature gridding is shown, in subplots a-c, to create large artificial anomalies away from constraint points (low values in upper right corners). These gridding artifacts result in large errors in the resulting bathymetry 3.20i-k. The bi-harmonic spline griddler (last column in 3.20) is shown to produce a residual field which adheres to the constraints, has smooth curvature near constraints, and doesn't create large artificial anomalies. The effectiveness of this griddler is confirmed by the low RMS difference between the inverted and true bathymetry. With the bi-harmonic spline gridding techniques shown to be the most effective, the remainder of this chapter uses this gridding technique for the constraint point minimize method of regional separation.

3.4.3 Inversion results

Using the cross-validated bi-harmonic gridding method to separate the regional component of the gravity misfit, the resulting residual misfit was used in an inversion. The same gravity data cross-validation method of determining the optimal damping parameter is used (Figure 3.21). The optimal damping parameter was found to be 10^{-3} . The resulting inversion is shown in Figure 3.22. The inverted bathymetry had

²Note that the gridding processes creates the regional field (not shown in Figure 3.20), which when subtracted from the total misfit gives the residual field. The residual grid is affected by these gridding effects through the removal of the regional field.

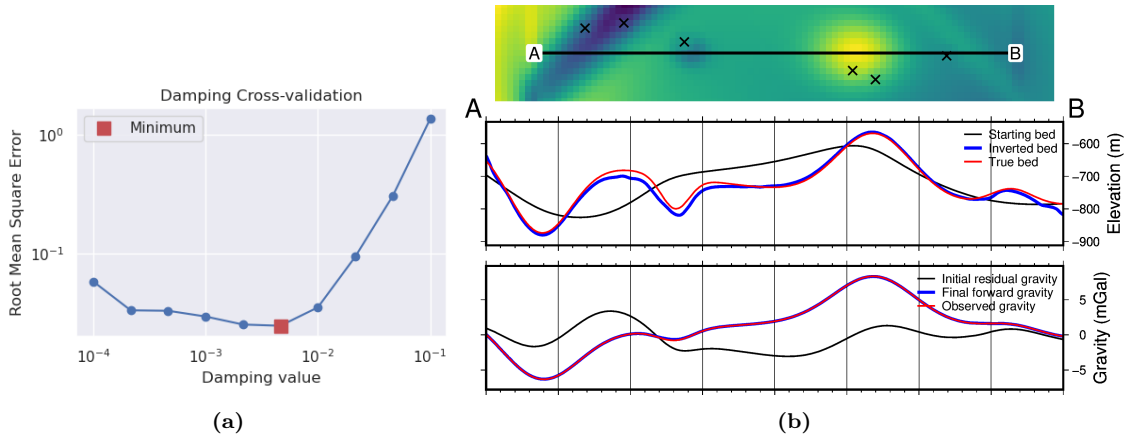


Figure 3.21: Cross-validation and profiles for the simple synthetic inversion with a regional component removed. **a)** Cross-validation curve showing the optimal damping parameter (red square). **b)** 2D profile of the inversion results. The top panel shows profile location and constraint points (black crosses). The middle panel contains topographic profiles of the starting, inverted, and true bathymetries. The bottom panel contains gravity anomaly profiles.

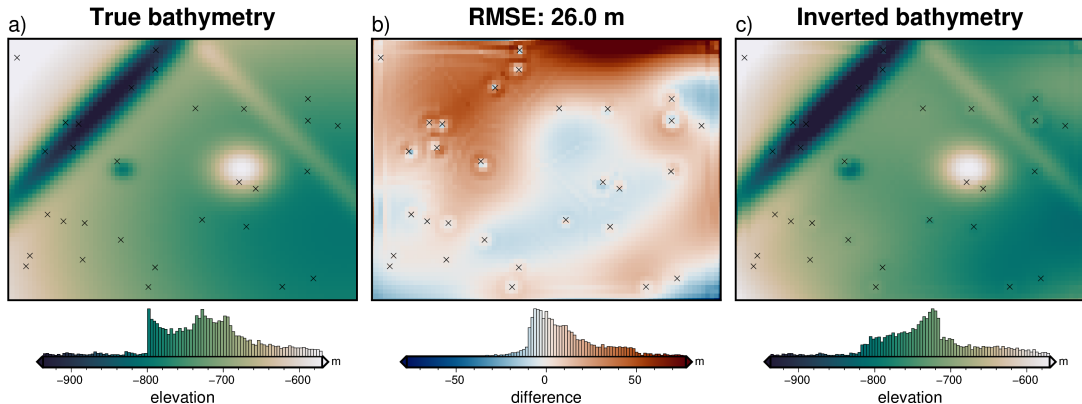


Figure 3.22: Simple synthetic model inversion with a removed regional component. **a)** True bathymetry, **b)** difference between a and c, **c)** final inverted bathymetry. Black crosses are constraint points. The RMS difference with the true bathymetry at these constraints is 2 m.

an RMS difference with the true bathymetry of 26 m, and an RMS difference at the constraints of 2 m. The inversion was completed in 79 seconds, with 38 iterations and a final RMS residual of 0.024 mGal. It terminated due to a lack of significant change in the ℓ^2 -norm at the final iteration. All four bathymetric features were recovered, but a lack of constraints in a few regions (the upper-right corner) lead to a miscalculation of the regional field, and a subsequent over-deepening of the bathymetry.

The regional separation, parameter cross-validation, and inversion was repeated with additive noise and re-sampling of the gravity data to a coarser resolution (Appendix B.1). As in section 3.3.2, this workflow was also repeated for an ensemble of noise levels and gravity data grid spacings, as discussed next.

3.4.4 Ensemble of Noise and Sampling values

Following the method outlined in Section 3.3.2, an ensemble of 100 inversions with varying levels of noise and gravity observation spacings are conducted. The noise and gravity spacing changes were applied to the original observed data, and the forward calculation of the starting model, initial misfit calculation, and regional field removal

Synthetic models statistics summary					
	RMS (m)	RMS at constraints (m)	Total time (hr:min:sec)	# iterations	Final residual (mGal)
No regional component					
Starting bathymetry	66	0.04	–	–	2.7
annulus	8	1	00:00:24	28	0.021
finite differences	9	2	00:03:00	37	0.022
2% noise	12	< 1	00:00:18	18	0.16
6 km re-grid	9	1	00:00:54	31	0.018
With regional component					
Starting bathymetry	66	0.04	–	–	7.4
filter	52	–	–	–	–
trend	66	–	–	–	–
equivalent sources	63	–	–	–	–
constraint point minimization	26	2	00:01:19	38	0.024

1196 were all repeated. Each model was then inverted with a cross-validation, and the
 1197 resulting RMS difference with the true bathymetry are shown in Figure 3.23.

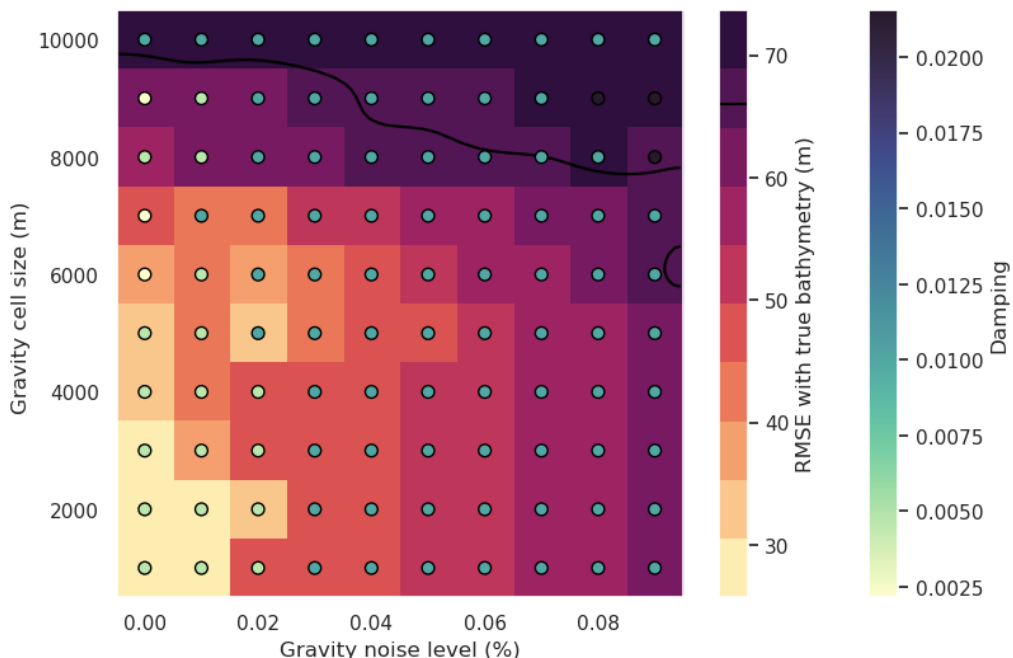


Figure 3.23: Ensemble of noise levels and gravity spacing for the simple synthetic model with a regional field. Grid cell color indicates each inversion's RMSE with the true bathymetry. Circles' color indicate the optimal damping value found for each inversion's cross-validation. Black line shows the 66 m contour, representing the RMS difference between the true and starting bathymetry.

1198 3.4.5 Simple model comparison

1199 Table 3.4.5 compares the performance of each of the above inversions. The four inversion
 1200 without a regional component of the gravity data all recovered the bathymetry
 1201 with an RMSE of ~ 10 m. With the regional component, the lowest RMS was
 1202 raised to 26 m. The constraint point minimization method of regional separation
 1203 produced significantly more accurate bathymetry models than the other methods.
 1204 With these optimal methods and baseline performance standards, a new synthetic
 1205 model is introduced which was created to emulate the expected bathymetry features
 1206 and gravity anomalies associated with a sub-ice shelf environment.

1207 3.5 Ross Sea model

1208 Here the last synthetic model is introduced, which is a semi-realistic model. In the
 1209 past section two synthetic topographies (bathymetry and a crustal layer) were used
 1210 in forward modelling to create synthetic gravity data. Here, real topographic data is
 1211 used to create the the synthetic gravity. This model is semi-realistic since the gravity
 1212 is synthetically calculated, but it results from geologically real surfaces. This model
 1213 uses data from Antarctica's Ross Sea (Figure 3.1, north of Ross Ice Shelf). The
 1214 bathymetry data is from the IBCSO v2 data compilation (Dorschel et al., 2022),
 1215 resampled at a 5 km resolution (Figure 3.24a). This data is mostly from shipborne
 1216 multi-beam echo sounding. To create the regional component of gravity, basement
 1217 depths from the ANTOSTRAT compilation of shipborne seismic data has been used
 1218 (Brancolini et al., 1995), at a 5 km resolution (Figure 3.24b). The inversion domain
 1219 is 320×420 km and a buffer zone of 40 km was included in all directions, resulting
 1220 in 8000 grid cells per surface.

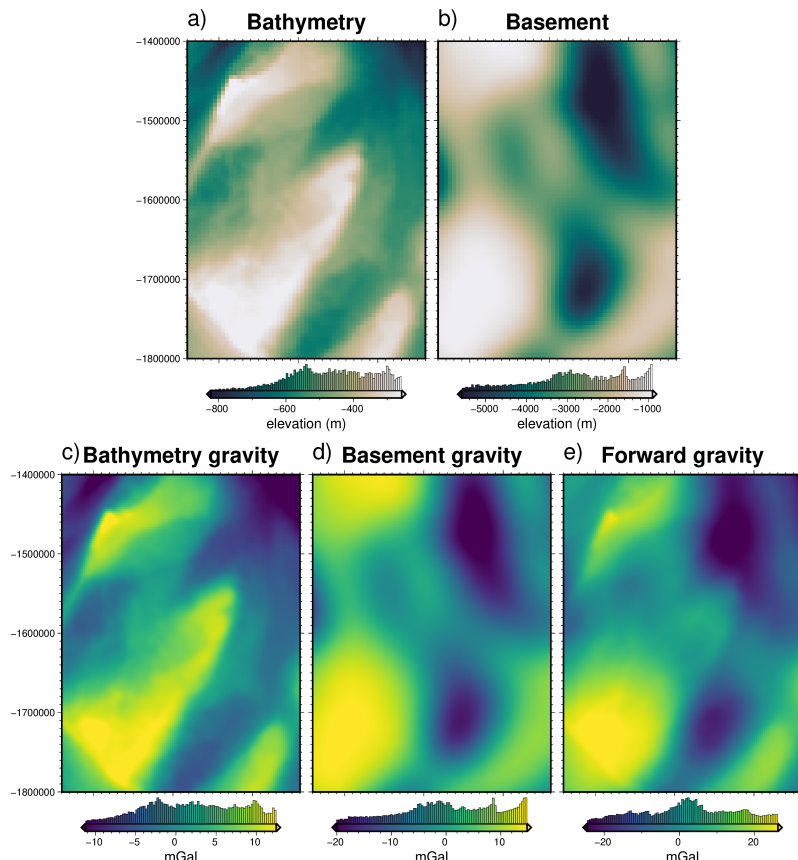


Figure 3.24: Ross Sea semi-synthetic model. **a)** Bathymetry data at 5 km resolution from IBCSO v2 (Dorschel et al., 2022), **b)** basement topography from the ANTOSTRAT project at 5 km resolution (Brancolini et al., 1995), **c)** forward gravity calculated at a regular 5 km grid at 1 km altitude for the bathymetry and **d)** for the basement. **e)** Total forward gravity from the combinations of c and d.

1221 Observed gravity

1222 These two surfaces were discretized with the reference discretization method (Figure
 1223 3.2e) with the mean elevation of each surface as its reference level. A density contrast
 1224 of $\Delta\rho = 1276 \text{ kg m}^{-3}$ (contrast between seawater(1024 kg m^{-3}) and sediment (2300

kg m⁻¹)), was used, with $+\Delta\rho$ for prisms above the reference, and $-\Delta\rho$ for prisms below the reference. For the basement, a density contrast of $\Delta\rho = 200 \text{ kg m}^{-3}$ was used, representing the contrast between sediment (2300 kg m^{-3}) and low-density rock (2500 kg m^{-3}). This contrast was set so that the resulting forward gravity of the basement was slightly greater in magnitude than that of the bathymetry. The forward gravity of each layer was calculated at a regular grid of observation points with a 5 km spacing, at a constant elevation of 1 km (Figure 3.24c-d). This created the full resolution synthetic observed gravity dataset. To represent an airborne gravity survey, this grid is sampled along synthetic flights lines.

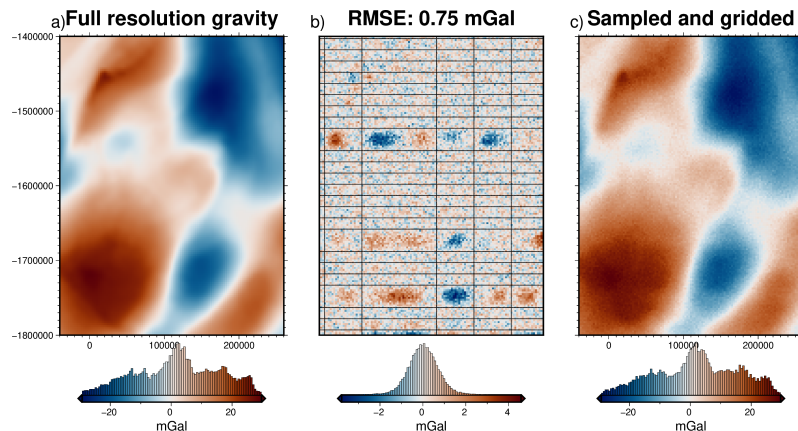


Figure 3.25: Ross Sea synthetic airborne survey. **a)** Full resolution gravity data from the forward calculation of the bathymetry and basement. **b)** Difference between a and b, with black lines showing the synthetic airborne survey points. **c)** Gravity data from a sampled along flight lines and re-gridded with equivalent sources.

This synthetic survey (Figure 3.25b) consisted of five N-S and 24 E-W flight lines. Spacing between lines was 50 km for the N-S lines and 15 km for the E-W lines. One N-S line and 3 E-W were omitted to represent missed flights. Along line spacing of data was 5 km. This survey configuration is similar to other Antarctic airborne surveys (Tinto et al., 2019). The full resolution gravity (Figure 3.25a) was sampled at these flight line locations, and the resulting values were fitted with equivalent sources. These gravity was then predicted from these sources on an even 5 km grid³ over the whole domain (Figure 3.25c). Lastly, the survey data was contaminated with noise from a Gaussian distribution, with a mean of 0 and a standard deviation of 0.6 mGal (2% of the max absolute value of the full resolution data). The difference between the true gravity and this noise-contaminated synthetic survey (Figure 3.25b) represents the typically loss of data resulting from a sparse airborne survey. The RMS difference is 0.75 mGal. The largest differences are located within the flight line data gaps.

Starting bathymetry

The bed elevations around the borders of ice shelves are generally well constrained. Bathymetry depths from the open ocean portion of the ice shelf border can be found through satellite altimetry or multi-beam sonar surveys. The remainder of the ice shelf border consists of grounded ice. Bed elevations beneath grounded ice can be efficiently imaged or modelled with methods such as airborne radar or mass-conservation modelling (Morlighem et al., 2020). Many Antarctic ice shelves also

³Actually on a 2.5 km grid to account for the testing data.

1255 contain sparse direct measurements of bathymetry from seismic surveying. This
 1256 resulting configuration for many ice shelves is generalized by a very well constrained
 1257 border with sparse constraints located within. Here, this configuration is mimicked
 1258 for hypothetic ice shelf in the Ross Sea.

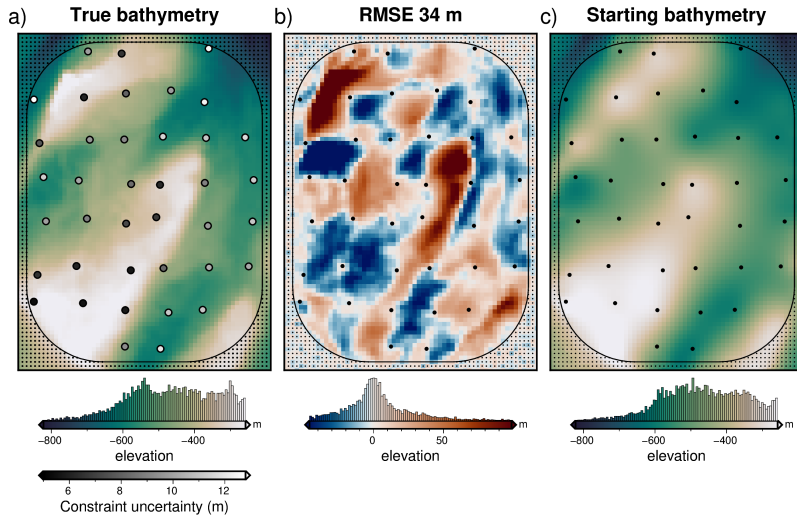


Figure 3.26: Gridding of the Ross Sea starting bathymetry. **a)** True bathymetry at 5 km resolution from the IBCSO v2 compilation (Dorschel et al., 2022). Constraint points (colored dots), show the uncertainty values of each point. There uncertainties were used as the standard deviations of Gaussian function for contaminated the sampled data with noise before re-gridding. **b)** Difference between a and b, and **c)** starting bathymetry from the sampling and gridding of the constraint points with added noise (black dots). Semi-rounded black line shows the outline of the synthetic ice shelf.

1259 Within the model domain, a polygon is created to represent the ice shelf bor-
 1260 der (Figure 3.26). Outside this border, constraint points are placed in each grid
 1261 cell of the model ($N = 3503$, small black dots in Figure 3.26). Within the border,
 1262 constraints are placed on a semi-regular grid. To represent a spatial constraint den-
 1263 sity similar to other Antarctic ice shelves⁴, 1 constraint per 2500 km^2 is used. This
 1264 equates to 39 constraints. In the previous models, the true bathymetry was sampled
 1265 at the constraints and the resulting values were gridded for the entire domain. Here,
 1266 to represent measurement uncertainties for attaining the constraint point depths, af-
 1267 ter each point is sampled, Gaussian noise is add to the values before gridding.

1268
 1269 Points outside of the ice shelf are contaminated with noise from a Gaussian dis-
 1270 tribution with a standard deviation of 5 m. This represents the well-constrained
 1271 methods associated with bed observations on either grounded ice or in the open
 1272 ocean. Points within the shelf are contaminated with noise based on their depth.
 1273 The Gaussian distribution used has a standard deviation of 2% of each points depth.
 1274 This simulates increasing measurement uncertainty with depth, a valid assumption
 1275 for techniques such as seismic surveying (probably need citation here, suggestions
 1276 Huw??). This equates to a RMS noise value of ~ 10 m for the ice shelf con-
 1277 straints. The uncertainty (the standard deviation of the Gaussian function used,
 1278 not the actual value of the noise) of each point is shown in Figure 3.26a. This
 1279 noise-contaminated sparse data is then gridded with a cross-validated bi-harmonic
 1280 spline yielding the starting bathymetry. This gridded takes the uncertainties of each

⁴ ~ 1 constraint per 2200 km^2 for the Ross Ice Shelf

point into account so that highly uncertain points don't introduce a bias into the interpolation (Uieda, 2018). The difference between the true and starting bathymetries (RMS of 34 m) shows the typically error expected for many ice shelves with only sparse constraints. The RMS between the constraint values within the ice shelf (noise-contaminated) and the true bathymetry is 10 m.

Gravity misfit

The starting bathymetry was discretized and forward modelled at the observation points with a density contrast of 1276 kg m^{-3} . This forward gravity was then subtracted from the observed gravity to get the gravity misfit (Figure 3.27a). Using the constraint point minimization method, the regional field was estimated with a bi-harmonic spline gridded (Figure 3.27b), which was subsequently removed, leaving the residual misfit (Figure 3.27c). As in the above section, the gridded takes the uncertainty of each constraint point into account to avoid overfitting the regional field to highly-uncertain constraint points.

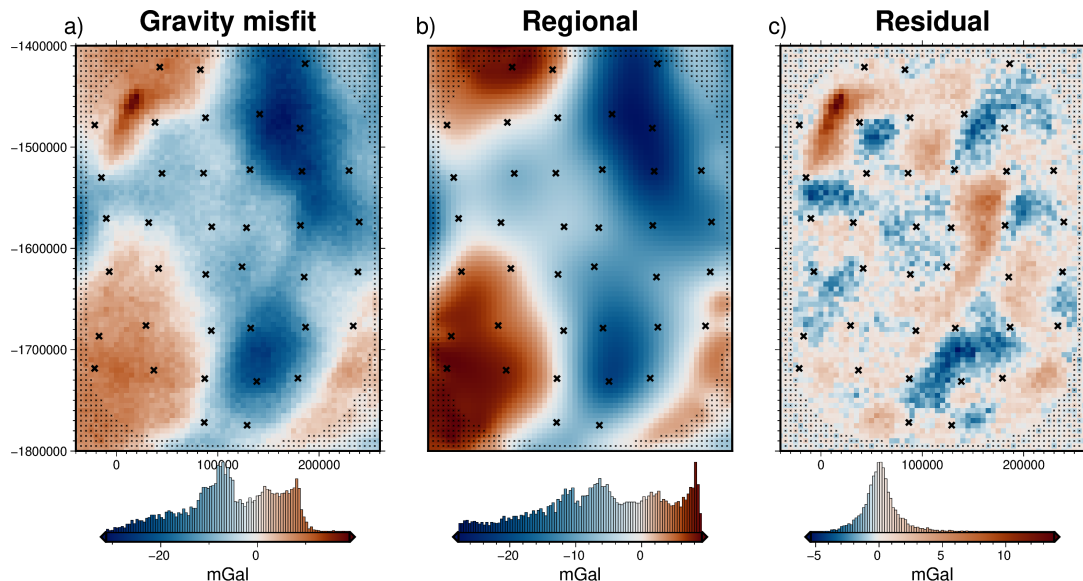


Figure 3.27: Ross Sea synthetic gravity anomalies, **a)** total gravity misfit, **b)** the estimated regional component using the constraint point minimization method, and **c)**, the residual misfit, as the difference between the total misfit and the regional component. Black crosses, large and small, show constraints inside and outside the ice shelf, respectively.

Inversion

This residual misfit was then used in a cross-validation of 16 damping parameter values (Figure 3.29a). The inversion with the lowest cross-validation score was then chosen as the best model. During the inversions a weighting grid was used to constrain the bathymetry at the points of known depths. This grid (Figure 3.28) is a normalized (0-1) grid of the minimum distance between each grid cell and the nearest constraint point. The inversion results, and the difference from the true bathymetry is shown in Figure 3.30. The inversion had a RMS difference with the true Ross Sea bathymetry of 21 m, and an RMS at the constraints of < 1 m. The inversion converged in 8 seconds at 15 iterations and had final residual misfit of 0.43 mGal.

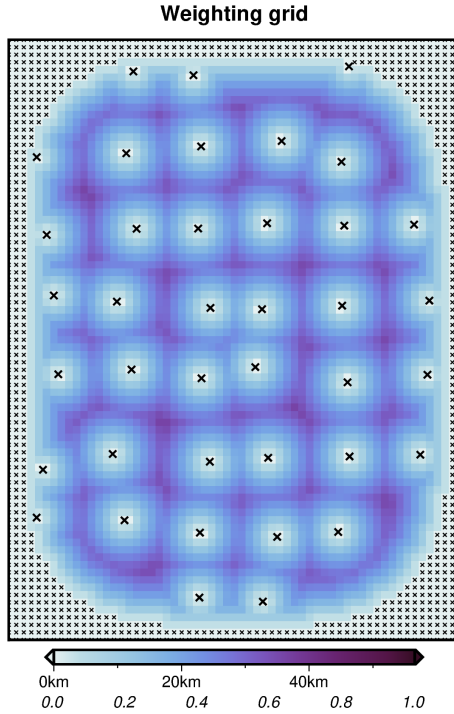


Figure 3.28: Weighting grid calculated from the minimum distance between each grid cell and the nearest constraint point. These distance are then normalized from 0 to 1.

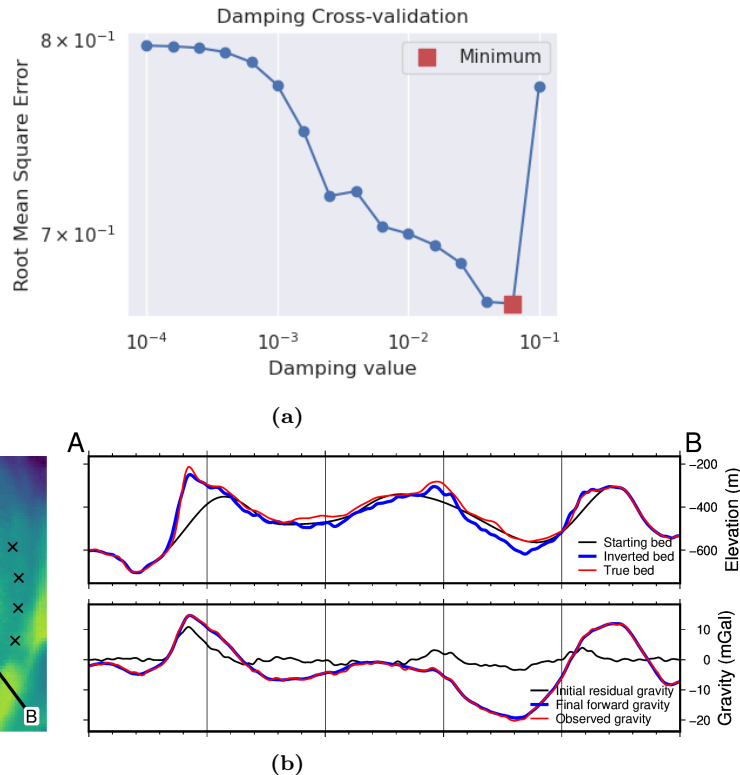


Figure 3.29: Cross-validation and profiles for the Ross Sea synthetic inversion with a regional component removed. **a)** Cross-validation curve showing the optimal damping parameter (red square). **b)** 2D profile of the inversion results. The top panel shows profile location and constraint points (black crosses). The middle panel contains topographic profiles of the starting, inverted, and true bathymetries. The bottom panel contains gravity anomaly profiles.

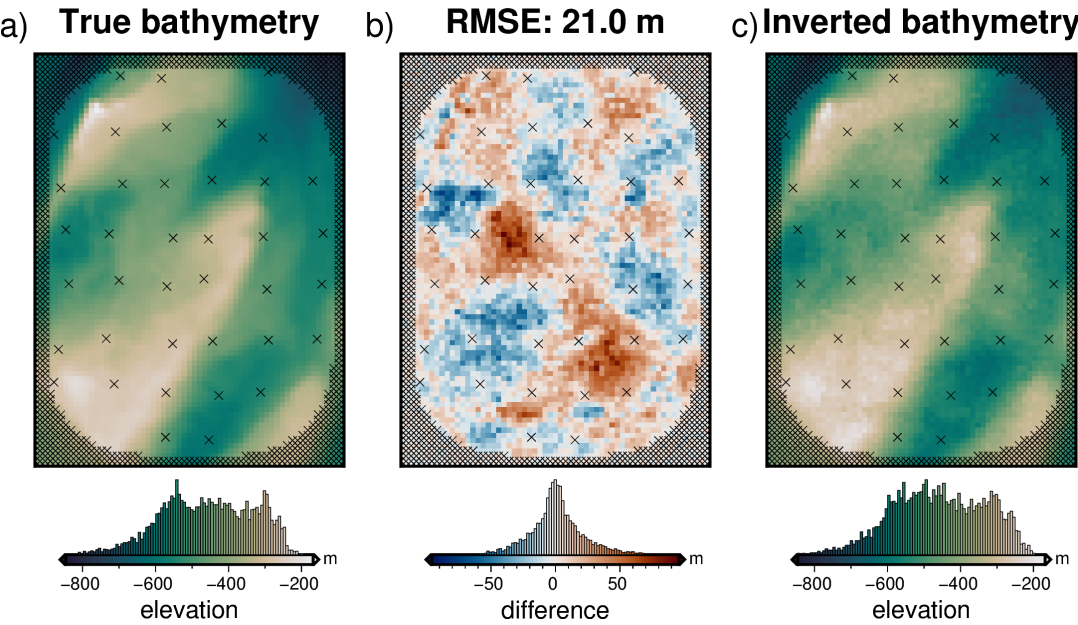


Figure 3.30: Ross Sea synthetic model inversion results. **a)** True bathymetry, **b)** difference between a and c, and **c)** final inverted bathymetry. Black crosses are constraint points. The RMS difference with the true bathymetry at these constraints is < 1 m.

1306 Uncertainty analysis

1307 Since the true Ross Sea bathymetry for this inversion is known, a direct measurement
 1308 of the spatial uncertainty of the resulting bathymetry is simple to calculate
 1309 (Figure 3.30b). This spatial uncertainty is vital to provide alongside the bathymetry
 1310 results. It informs ocean modellers where results can be confidently interpreted and
 1311 highlight regions to focus future data collection. Here, a method of uncertainty
 1312 analysis for this inversion is proposed, and the resulting uncertainty is compared to
 1313 the inversion error to get a sense of the accuracy of our calculation of uncertainty.
 1314 This uncertainty analysis is accomplished with Monte Carlo simulations.

1315
 1316 Here, 100 inversions are run with the gravity data and optimal damping parameter
 1317 from the above inversion. Each inversion contains input parameters which
 1318 are randomly sampled from distributions of their possible values. These prior
 1319 distributions represent all plausible parameter values and thus the resulting inverted
 1320 bathymetries should cover the range of plausible inversion outcomes. For each grid
 1321 cell, the weighted standard deviation of the 100 inverted bathymetry values of that
 1322 grid-cell were calculated. The weighting came from the inverse square of each inversion's
 1323 RMS of the final gravity misfit. This reduces the bias from inversions with
 1324 large misfits (Schnaidt & Heinson, 2015). The parameters included in the Monte
 1325 Carlo sampling are:

- 1326 1. the observed gravity data, sampled from a normal distribution with a mean
 1327 equal to the observed values and a standard deviation of 0.6 mGal (2% of the
 1328 maximum absolute value).
- 1329 2. the constraint point depths, sampled from a uniform distribution with a center
 1330 as the measured point depth and bounds of ± 5 m for the points outside the
 1331 ice shelf, and $\pm 2\%$ depth for points within the shelf.
- 1332 3. the bathymetry density contrast. This is defined as the difference between the

1333 densities of water and sediment. Water density was sampled from a normal
 1334 distribution with a mean of 1024 kg m^{-3} and a standard deviation of 5 kg m^{-3} .
 1335 Sediment density was sampled from a distribution with a mean of 2300 kg m^{-3}
 1336 and a standard deviation of 400 kg m^{-3} .

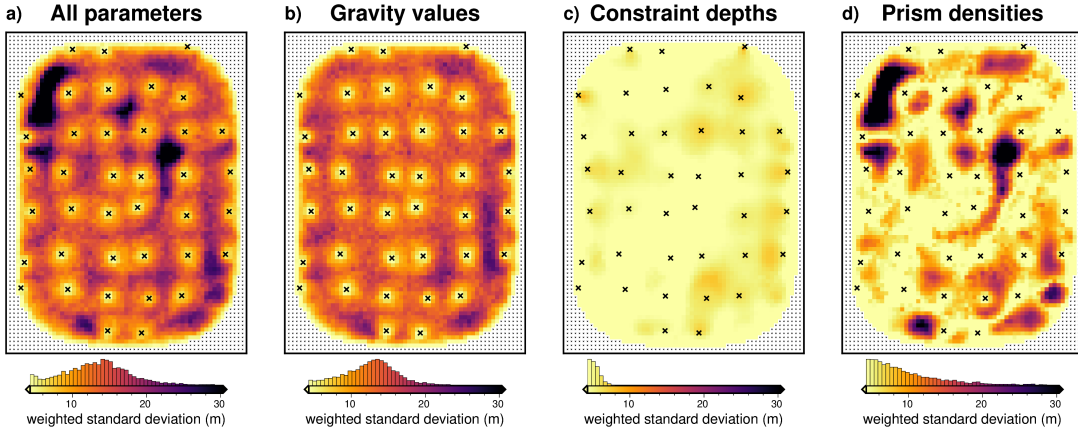


Figure 3.31: Monte Carlo simulation results for the Ross Sea synthetic inversion. Cell-wise weighted standard deviations of all 100 inversions in each simulation. **a)** Monte Carlo simulation with pseudo-random sampling of the gravity data values, the constraint point depths, and the prisms density values. **b)** Sampling of only the gravity data values. **c)** Sampling of only the constraint point depths. **d)** Sampling of only the density values. All plots share the same colormap. To aid in interpretation, locations outside of the ice shelf have been masked. Constraints outside of the ice shelf are shown as small black crosses and constraints within the ice shelf are shown as large black crosses.

1337 Four Monte Carlo simulations were run and are shown in 3.31. Each of the
 1338 above parameters; gravity, constraints, and densities, were included in their own
 1339 Monte Carlo simulations, and the fourth simulation included all parameters to-
 1340 gether. Simulations which included the sampling of the constraint depths required
 1341 the re-calculation of the starting bathymetry, the starting forward gravity, gravity
 1342 misfit, regional separation, and finally running the inversion. Simulations which in-
 1343 cluded sampling the density values required recalculating the forward gravity, misfit,
 1344 regional separation and running the inversion. Simulations which included the sam-
 1345 pling of gravity values only required recalculating the regional field and running the
 1346 inversion.

1347 Effects of constraint spacing

1348 Here we test the effects of the number and spacing of constraint points on the
 1349 accuracy of the inversion. The constraints outside the ice shelf are kept as they have
 1350 been in the previous section, at the same grid spacing as the bathymetry (5 km).
 1351 Constraints within the ice shelf are re-created on a regular grid, where the spacing of
 1352 the grid, and thus the number of constraints, is varied from 10 km (959 constraints)
 1353 to 100 km (9 constraints). The depth of the true bathymetry is sampled at each
 1354 constraint. As in the previous section, points outside the shelf are contaminated with
 1355 Gaussian noise with a standard deviation of 5 m. Noise for constraints within the
 1356 ice shelf is relative to each points depth (to simulate seismic survey uncertainties).
 1357 These noise-contaminated constraint point depths are used in a bi-harmonic spline
 1358 gridding to create the starting bed for each of the 10 constraint sets. The RMS
 1359 difference between each of the starting beds and the true bed is shown as green dots

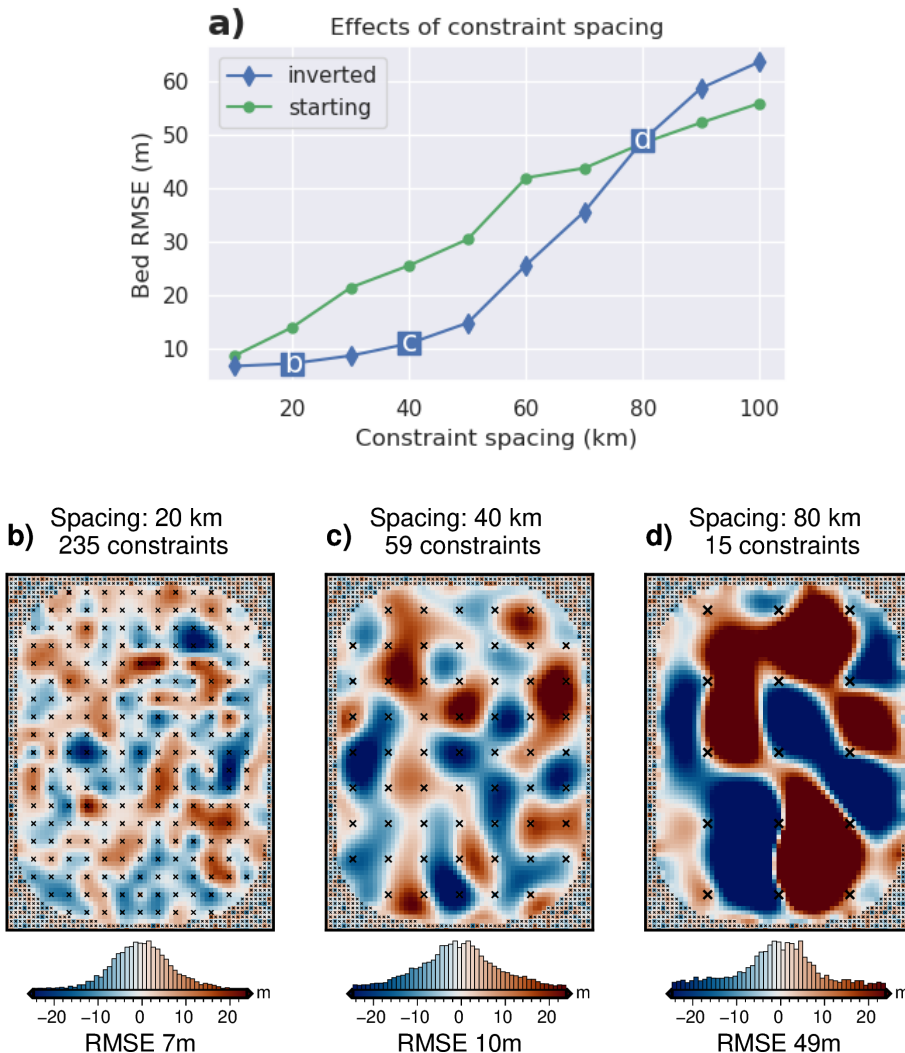


Figure 3.32: Effects of constraint spacing on inversion accuracy. **a)** Bathymetry error (RMSE) relative to the true bathymetry for 10 different constraint spacing's. Green (circles) shows the starting error and blue (diamonds) shows the error after inversion. Labels b, c, and d refer to the three inversion error results shown as subplots. **b-d)** Inversion error grids for three of the ten configurations of constraints (labeled on a)). Note b-d use the same colormap. Small black crosses show constraints outside the ice shelf, and larger black crosses show inside constraints with the corresponding constraint spacing.

1360 in Figure 3.32a. From these starting beds the inversion workflow was conducted, as
1361 below:

- 1362 1. the forward gravity of the starting beds were calculated,
- 1363 2. the misfits with the observed gravity (Figure 3.25a) were calculated⁵
- 1364 3. the regional component of the misfit was estimated and removed with the
1365 constraint point minimization method
- 1366 4. the residual misfit was inverted with the cross-validation routine

⁵To isolate the effects of changing the constraint density, the full resolution observed gravity with no added noise was used here, instead of the synthetic survey gravity.

1367 5. the difference between each inverted bed and the true bed was found

1368 Figure 3.32 shows the results of this analysis. Subplot a) shows the relationship
1369 between constraints spacing and the RMSE with the true bed of the starting bed
1370 (green circles) and the final inverted bed (blue diamonds). Three of the inverted
1371 bed errors are shown in subplots b-d. See Appendix B.2 for plots of the regional
1372 separation errors for these three inversions.

1373 3.5.1 Effects of gravity data

1374 As the above section analyzed the impact of the number of constraint points on the
1375 inversion's accuracy, here we investigate the impact of the quality and quantity of
1376 input gravity data. Following the methods of the two ensembles presented in the
1377 simple synthetic inversion (Figure 3.3.2 & 3.23), an ensemble of 100 inversions with
1378 varying levels of noise and gravity observation spacing's are conducted with this Ross
1379 Sea model. The observed gravity data was contaminated with noise as described
1380 in the past sections, with 10 levels between 0 and 9% of the max absolute value (0
1381 - 2.7 mGal). To simulate a more spare gravity survey, the previous two ensembles
1382 sampled the full resolution gravity data onto a coarser evenly spaced grid and then
1383 re-gridded the sparse data with equivalent sources back to the full resolution of the
1384 bathymetry. Here instead of evenly spaced grids, we use airborne flight lines.

1385

1386 We use a constant along-line observation spacing of 5 km, but vary the spacing
1387 between flight lines. The N-S and E-W lines both use the same between-line spacing.
1388 The full resolution gravity is then sampled at these points, and the sparse data is
1389 re-gridded to the full resolution (5 km) with equivalent sources. The noise and
1390 line spacing changes were applied to the original observed data, and the forward
1391 calculation of the starting model, initial misfit calculation, and regional field removal
1392 were all repeated. Each model was then inverted with a cross-validation, and the
1393 resulting RMS difference with the true bathymetry are shown in Figure 3.33.

1394 3.6 Discussion

1395 3.7 Simple synthetic model

1396 The simple synthetic model of Section 3.3.1 was introduced to 1) present the basic
1397 workflow of the inversion, 2) determine the best options for various components of
1398 the inversion and 3) demonstrate the capabilities and limitations of the inversion.
1399 The starting bathymetry had a RMS difference with the true bathymetry of 66 m
1400 (Figure 3.6). This error demonstrates the limitations of gridding sparse data. Even
1401 with a very high spatial constraint density (1 constraint per 160 km²) compared
1402 to most ice shelves (need a reference or figure here???), simply gridding the con-
1403 straints greatly misinterpreted the true bathymetry. To reduce this bathymetric
1404 error, we presented three inversions, a noise-free full-resolution inversion, a noise-
1405 contaminated full resolution inversion, and a noise-free lower resolution inversion.

1406 Inversion results

1407 All of these inversions were able to reduce this RMS difference with the true bathymetry
1408 to ~ 10 m, and recover all bathymetric features of interest. We demonstrated that

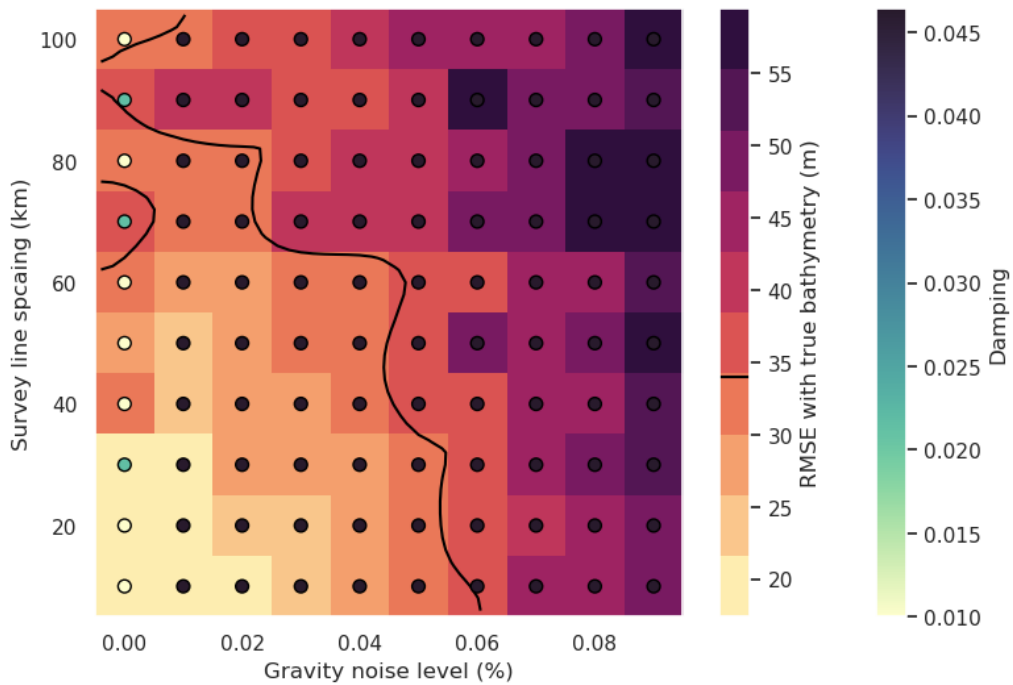


Figure 3.33: Ensemble of noise levels and airborne gravity line spacing for the Ross Sea synthetic model. Grid cell color indicates each inversion's RMSE with the true bathymetry. Circles' color indicate the optimal damping value found for each inversion's cross-validation. Black line shows the 34 m contour which represents the RMS difference between the true and starting bathymetry (Figure 3.26b).

the two method of calculating the vertical derivative of gravity produced similar results, but the annulus approximation was significantly quicker ($\sim 6\times$). Additionally, for each of these inversions, the weighting grid, based on the distance to the nearest constraints (Figure 3.5), successfully constrained the resulting inverted bathymetry at the points of prior bathymetry observations. Each inversion's constraint point RMS difference with the true bathymetry was $<\sim 2$ m, and the technique avoided any pedestal effect around the constraints in the resulting bathymetries. Interestingly, the noise-free low-resolution inversion resulting in the lowest RMS difference with the true bathymetry (Figure 3.15). This inversion used gravity data on a 6 km grid, instead of the full resolution of 1 km used in the other inversions. This demonstrates that high resolution gravity surveys may not be necessary to achieve adequate results from an inversion.

Ensemble results

To test this theory further, we conducted an ensemble of 100 inversions with 10 levels of noise-contamination and 10 gravity survey resolutions. The resulting RMS difference of each inversion with the true bathymetry is shown in Figure 3.17. All inversions in this ensemble, including the worst case scenario of 9% noise and a gravity observation grid of $10\times$ the bathymetry spacing, still resulted in an RMS differences lower than that of the starting bathymetry (66 m). It is worth noting that this metric for the accuracy of the inversion, the root mean squared (RMS) difference with the true bathymetry, is used to give extra weighting to the outlier errors, as opposed to using a mean average error (MAE). These outliers typically include the features of interest in a bathymetry inversion. Figure 3.34a shows these ensemble results grouped by cell size. For each cell size value (color of lines), the

inverted bed RMSE for the range of noise levels are shown. This shows a roughly linear relationship between noise and RMSE, regardless of cell size. Conversely, figure 3.34b shows these ensemble results grouped by noise level. For each noise level (color of lines), the inverted bed RMSE for the range of cell sizes are shown. This shows an exponential relationship between survey resolution and RMSE. This exponential relationship is strongest for low noise levels. The close spacing of the low-cell-size lines (purples) in Figure 3.34a show the diminishing improvements once the gravity resolution is at or below ~ 5 km. Conversely, there is a continuous improvement on the inversion error with lower levels of noise.

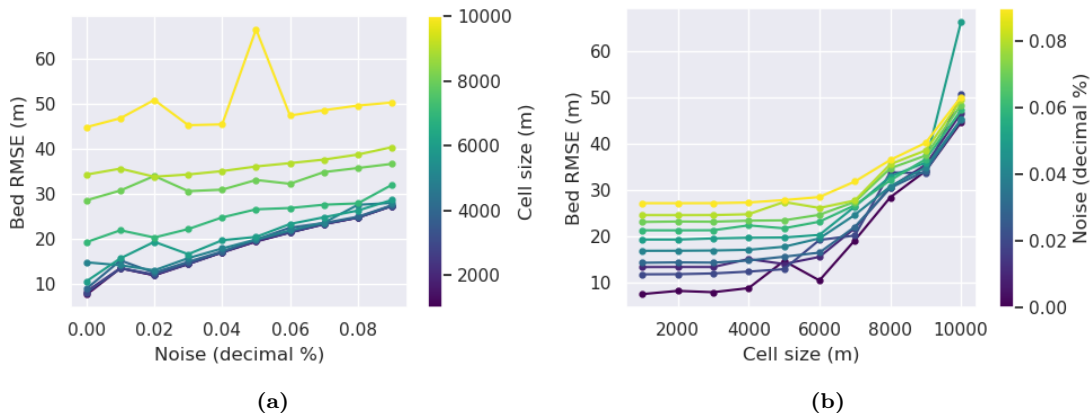


Figure 3.34: Ensemble results for the simple synthetic inversion, grouped by **a)** gravity survey cell size, and by **b)** noise level. Each line in a) corresponds to a row of Figure 3.17 and each line in b) corresponds to a column.

In a typically gravity survey there is often a trade-off between the number of observations made and the quality (noise) of the data. This is due to the time restrictions of both the total data collected period (i.e. the length of a field-season in Antarctica), and the necessity to repeat base-station measurements to account for instrument drift. To collect more data in the same time inevitably results in increased noise. At a certain point, this increased noise will have a greater negative effect on the inversion results, than will be counteracted by the increase amount of data. These are important consideration for survey design. Figure 3.34b shows that for a given noise level, there is little benefit in increasing the gravity survey resolution from ~ 6 km to 1 km. For this survey domain (60×80 km), a 6 km resolution results in ~ 130 gravity station, while with a 1 km resolution this increases to 4800 observations points. Simplistically speaking, if keeping total survey time constant, this means at 6 km spacing as opposed to 1 km spacing, either $\sim 36\times$ more area could be surveyed, or higher quality data could be collected, with shorter basestation loops, more repeated ties, and more careful measurements.

1457

The results from the noise-contaminated inversion (Figure 3.12 & 3.9b) show that this gravity noise is directly reflected in the inversion results. For this reason, data, either the observed data or the residual misfit, is typically low-pass filtered prior to inversion (i.e. Boghosian et al., 2015; Yang et al., 2020). This is typically done with either a time based filter for airborne surveys, or a spatial filter. With this filtering there is a trade off between removing the noise, and removing the true signal. Due to this, we have chosen to omit the filtering in these synthetic examples.

3.8 Simple model with a regional component

Regional separation methods

The addition of a regional component to the observed gravity data adds a major complexity to the inversion workflow. The actual inversion remains the same, but this regional component must be estimated and removed beforehand. We tested four methods of regional estimation; 1) a low-pass filter, 2) fitting a polynomial trend to the data, 3) predicting the data with a set of deep point sources, and 4) attributing the entire misfit value to the regional field at constraint points and interpolating between these values. Figure 3.19 compares the inversion results of each of these methods. While each method recovered the short wavelength bathymetry features, the mis-estimation of the true regional field for each method introduced long-wavelength errors in the inversion results. We show that the constraint point minimization method most accurately estimated the region, and thus produced the best inversion results. For the simple regional field used here, the filter and trend methods achieved reasonable results, but the effectiveness of these methods is expected to be reduced with more complex regional fields associated with real data.

While the constraint point minimization worked best for this model, each of these methods may work better in specific scenarios. All the methods except the equivalent source method require the gravity data to be gridded over the entire region of interest. For sparse gravity surveys the interpolation required may introduce large errors. For this scenario, the equivalent source technique is likely the most appropriate. In scenarios with few bathymetry constraints and where the regional field is expected to be simple, the trend and low-pass filter methods are efficient and can be effective. However, if there are distributed bathymetry constraints, such as in this synthetic scenario, the constraint point minimization is likely the best choice. This technique will only effectively remove regional anomalies with a wavelength equal to or greater than the average constraint spacing. If the constraints are sparse relative to the expected regional anomaly wavelengths, this method will underestimate the regional component. Lastly, if the bathymetry contains long-wavelength features which would result in long wavelength anomalies, the trend, filter, and equivalent source techniques may include these in the regional removal. Therefore, the inverted bathymetry, while recovering the super-imposed short wavelength bathymetry features, will underestimate the long-wavelength features. It is for these reasons that the regional separation is the most important aspect of a bathymetry inversion.

Constraint point minimization

This constraint point minimization technique requires the gridding of sparse measurements of the regional field. We explored the impact of this gridding process on the resulting inversion. Figure 3.20 shows the results of four different gridding processes. Minimum curvature gridding without tension (tension of 0, Figure 3.20a) produces a smoothly varying surface at the constraints, but introduces artificial minima and maximum at points far from any constraints. This erroneous effect is minimized with a higher tension factor. Using a tension factor of 1, figure 3.20c shows the limited erroneous minima and maxima, but this added tension results in high gradients in the surface immediately near the constraint points (Figure 3.20g). These high gradients in the resulting residual anomalies create a *ringing* effect in

the inverted bathymetry (Figure 3.20k). For these reasons, an intermediate tension factor of 0.25 is suggested for potential fields data. While this limits the negative effects of both low and high tension, there are still false minima and maxima (Figure 3.20b), and high gradients at the constraints (Figure 3.20f). The last gridding technique uses bi-harmonic splines. The optimal parameters associated with this technique are chosen from a cross-validation of the constraints points. This technique, while being more computationally expensive, solves both issues of tensioned minimum curvature.

1519 Inversion results

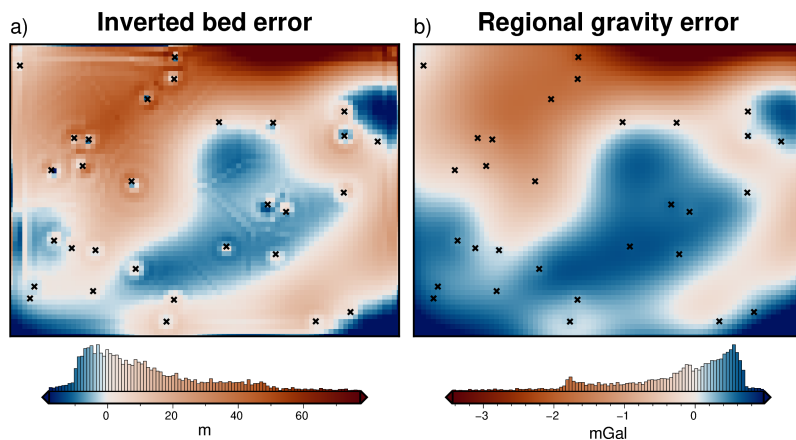


Figure 3.35: Source of inverted bathymetry error for the simple synthetic model with a regional field. **a)** Inverted bathymetry error from Figure 3.22b. **b)** Error in the estimation of the regional component of gravity from comparison with the true regional component (Figure 3.18b). Black crosses show constraint points. Colormaps are opposed to highlight the similarities and the median has been removed from the regional error.

With both the optimal regional separation method and the optimal gridding method determined, we performed a cross-validated inversion with the remaining residual misfit. This inversion was able to recover all the short-wavelength bathymetry features, but introduced some long-wavelength errors. Figure 3.35 shows the inverted bathymetry error alongside the error in estimating the regional component of gravity. Comparing these shows that almost all of the inverted bathymetry error is tied to the inaccuracies of determining the regional component. The remaining error are all minor short-wavelength features, mostly around constraint points. They appear to result from the weighting grid implementation of regularization. Since the errors in the regional estimation are the dominant source of error in most inversions, as shown above and by other Antarctic bathymetry inversions (Brisbourne et al., 2014), we believe these details of the gridding processes is a vital and often overlooked step in many studies.

1533 Ensemble results

As with the simple model, an ensemble of noise and gravity survey spacing was performed with this model containing a regional component. The lowest resulting RMS difference with the true bathymetry was raised from values of ~ 10 m for the inversion without the regional component, to a lowest value of ~ 25 m with the additional regional component. The black line in Figure 3.23 shows the 66 m contour, which represents the RMS difference between the true and starting bathymetries.

1540 Inversions which fall outside of this line resulted in a worse bathymetry than the
 1541 starting model. This shows that for this model, inversion are only worth conducting
 1542 if the gravity surveys has a spacings less than ~ 8 km ($\sim 8 \times$ the bathymetry spacing).
 1543 Figure 3.36 show these ensemble results grouped by cell-size and noise level. There
 1544 is a linear relationship between gravity noise and the resulting bathymetry RMSE,
 1545 for all gravity survey spacings. There is an approximately exponential relationship
 1546 between gravity survey cell size and resulting bathymetry RMSE. The degree of this
 1547 exponential relation decreases with increased noise.

1548

1549 For this model, the *elbow* of the exponential curves in Figure 3.36 is at $\sim 6 -$
 1550 8 km survey resolutions ($6-8 \times$ bathymetry resolution). This suggest that below a
 1551 survey resolution finer than ~ 8 km, there is little benefit in collecting more data.
 1552 This is supported by the close spacing of low-cell-size lines (purples) in Figure 3.36a.
 1553 Effort would be better spent collect data over a wider region, reducing noise in the
 1554 data, or if possible collecting more bathymetric constraints.

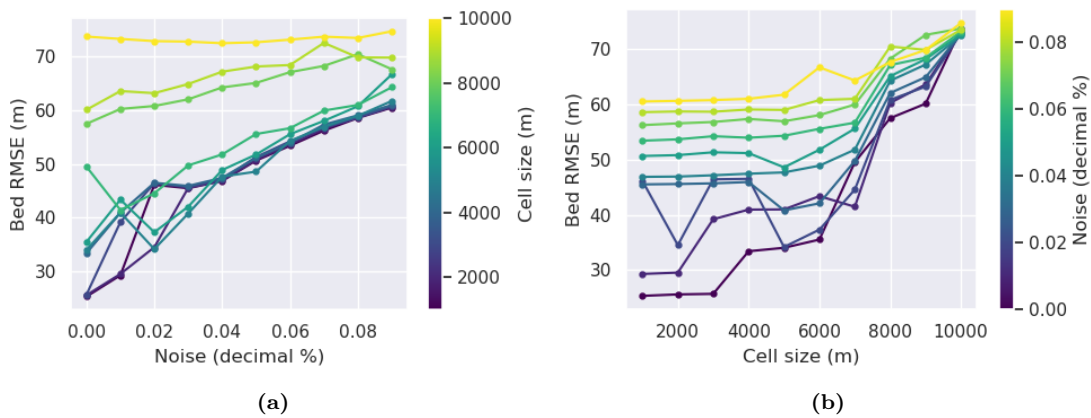


Figure 3.36: Ensemble results for the simple synthetic inversion with a regional component, grouped by **a**) gravity survey cell size, and by **b**) noise level. Each line in a) corresponds to a row of Figure 3.23 and each line in b) corresponds to a column.

1555 3.9 Ross Sea model

1556 The Ross Sea semi-realistic model was created to better emulate the gravity and
 1557 bathymetries expected for ice shelves. A few extra complexities were added to this
 1558 model compared to the past models. An ice shelf border was included, with a
 1559 high density of constraints outside of the border, and sparse constraints within. All
 1560 the constraints had an associated uncertainty, instead of directly sampling the true
 1561 bathymetry depths. The observed gravity was calculated along the flight paths of a
 1562 typical airborne survey, instead of along a uniform grid. The main inversion in this
 1563 section had 2% noise added, and had flight lines with 50 km N-S spacing and 15
 1564 km E-W spacing. The inversion successfully reduced the starting bathymetry error
 1565 from an RMSE of 34 m to 21 m. The resulting bathymetry shows a recovery of
 1566 most of the lost bathymetry features, but some noise from the gravity data has been
 1567 introduced into the bathymetry. Sharp bathymetry features (upper left corner) and
 1568 smooth features were both recovered. The constraint points were relatively evenly
 1569 distributed (Figure 3.28), resulting in a relatively even distribution of bathymetry

1570 misfits.

1571

1572 Of these errors, the largest were located at the gaps in the synthetic survey
 1573 where there were missing flight lines (Figure 3.25b). To understand the cause of
 1574 the remaining errors, we compare the inverted bathymetry error with the regional
 1575 separation error (Figure 3.37). The strong correlation between these two grids shows
 1576 that the majority of errors in the inversion are tied to the miscalculation of the
 1577 regional field, as was seen in the simple synthetic inversion with a regional field.
 1578 The remaining errors appear to be from the flight line gaps and noise in the gravity
 1579 data.

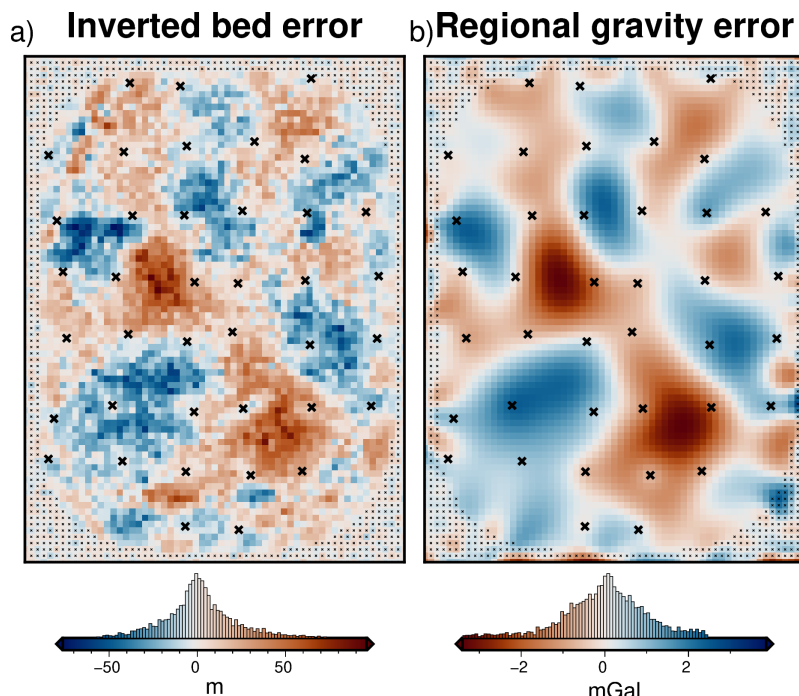


Figure 3.37: Comparison of the inverted bathymetry error and the error in the regional field estimation. **a)** Inverted bathymetry error from Figure 3.30b. **b)** Error in the estimation of the regional component of gravity from comparison with the true regional component (Figure 3.24d). Black crosses show constraint points. Colormaps are opposed to highlight the similarities and the median has been removed from the regional error.

1580 Effects of the gravity data

1581 The ensemble of gravity data noise levels and flight line spacings from Section 3.5.1
 1582 shows the relative importance of these two aspects of a gravity survey. As for the
 1583 previous ensembles, Figure 3.38 shows these results grouped by line spacing and by
 1584 noise level. For the Ross Sea model, both factors have a roughly linear relationship
 1585 with inverted bathymetry error. The slopes for the lines of best fit for Figure 3.38a
 1586 and b means the inversion RMSE increase by ~ 3 m for either a 1% increase in the
 1587 noise level or a 20 km increase in the average flight line spacing. The inversions
 1588 with a small line-spacing (purple lines) of Figure 3.5.1a are closely group, relative
 1589 to the higher line spacings. This shows that at already low line spacings (40 km)
 1590 there may be little benefit to reducing the line spacing further. Conversely, there
 1591 is a larger spread for the low noise inversions (purple lines) in Figure 3.5.1b. This
 1592 shows that even at low noise levels, further decreases may still provide important
 1593 improvements to the inversion outcome. As in the previous ensemble results, for

1594 a field application this demonstrates the important tradeoff between quantity and
 1595 quality of gravity data.

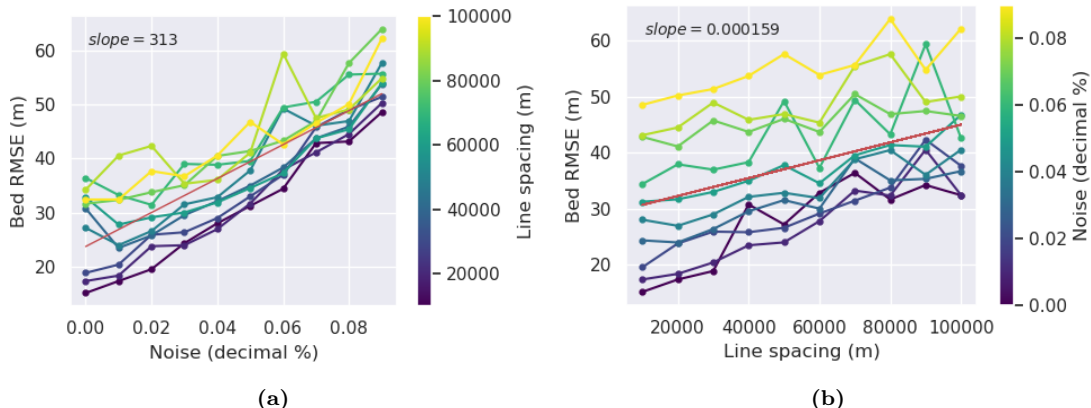


Figure 3.38: Ensemble results for the Ross Sea inversion, grouped by **a)** gravity survey line spacing, and by **b)** noise level. Each line in a corresponds to a row of Figure 3.33 and each line in b corresponds to a column. Red lines show the line of best fit, with their slopes shown in the upper left corners.

1596 These specific relationships between noise, line spacing, and inversion error, while
 1597 not application to all survey configurations, shows the importance of choosing an
 1598 appropriate survey design. This analysis with synthetic data could be included in a
 1599 pre-survey plan, to explore the effects of differing survey configurations.

1600 Effects of the constraints

1601 These synthetic inversions have shown that the removal of the regional field pre-
 1602 sented the biggest challenge for gravity inversions for bathymetry. The most robust
 1603 technique for removing the regional field requires a distribution of points of known
 1604 bathymetry across the ice shelf. Since the largest errors in the inverted bathymetries
 1605 occur at the largest distance to constraints, an even distribution of constraints will
 1606 best be able to estimate the regional field. Section 3.5 explored the effects of varying
 1607 the numbers of constraints, while keep the remaining components of the inversion
 1608 constant. Figure 3.32a shows the bathymetry RMSE with the true bathymetry both
 1609 before (green) and after (blue) the inversion is conducted.

1610
 1611 This shows for this synthetic model that for average constraint spacing's less than
 1612 ~ 20 km there is little improvement made by running an inversion. This is due to the
 1613 starting bathymetry model already being relatively accurate, with the inversion only
 1614 producing minor adjustments between constraint points. On the other end of the
 1615 spectrum, with constraint densities greater than ~ 70 km, the inverted bathymetry
 1616 has an error similar or higher to the un-inverted bathymetry. This is due to the
 1617 inaccuracies in calculating the regional field with only very sparse constraints. For
 1618 these scenarios, the errors introduced by the inversion are greater than the errors
 1619 of simply interpolating the constraint points. The slope of the inverted bathymetry
 1620 error curve shows that for this survey, once below a certain constraint spacing (~ 30
 1621 km) there is little benefit to having additional constraints.

1622 Uncertainties

1623 We have demonstrated that the majority of the inverted bathymetry error is related
1624 to the estimation of the regional component of gravity. Without knowing the true
1625 regional component, as we do in these synthetic examples, estimating the uncer-
1626 tainty in the interpolation between constraint points of the regional field is difficult.
1627 The uncertainty of each grid cell is strongly dependant on the distance to the near-
1628 est constraint, as well as the depth uncertainties of these nearby constraints. While
1629 this hasn't been implemented here yet, the field of conventional bathymetry surveying
1630 provides some tools to access the uncertainty of the gridding procedure (Bourgeois
1631 et al., 2016).

1632

1633 These account for both the depth uncertainty of each measurement, and the dis-
1634 tance of each grid cell to the nearest measurement. Future work will benefit from
1635 a quantitative assessment of the uncertainty of gridding the regional field from the
1636 constraint point values. While the uncertainty of the regional removal accounts for
1637 the majority of the uncertainty of the inverted bathymetry, it is technically com-
1638 pleted before the inversion and is thus not a component of the inversion uncertainty.
1639 To address the uncertainty resulting from the inversion process, we introduced a
1640 suite of Monte-Carlo simulations in Section 3.5.

1641

1642 These simulations each ran 100 inversion, with each inversion sampling plausible
1643 values of parameters used in the inversion. Gravity data, constraint depths, and
1644 water and sediment density were all sampled from their respective estimated ranges
1645 of uncertainties. We ran a full simulation of 100 samplings and inversions for each
1646 of these three parameters; gravity values, constraint depths, and prism densities.
1647 Additionally, we ran a fourth simulation sampling from all of these parameters. We
1648 interpret the cell-wise weighted standard deviations of these simulations as the un-
1649 certainty associated with each parameter. The results in figure 3.31 show a mean
1650 uncertainty for the entire region of ~ 15 m. The majority of this uncertainty is at-
1651 tributed to the uncertainty in the gravity data, shown by comparing the histograms
1652 3.31a and b.

1653

1654 The uncertainties in the gravity data result in a relatively uniform bathymetry
1655 uncertainty across the region of ~ 13 m. A simple calculation with the Bouguer
1656 slab formula with a density contrast of 1276 kg m^{-3} and the assumed gravity un-
1657 certainty of 0.6 mGal gives a similar value of 11.2 m ($\Delta g_{\text{boug}} = 4.18 \times 10^{-5} \rho h$). This
1658 uncertainty is lowest at the constraints, due to the use of the weighting grid in the in-
1659 version. The contribution to the bathymetry uncertainty from the depth uncertainty
1660 of the constraint points is small. The mean bathymetry uncertainty resulting from
1661 these constraint point uncertainties is ~ 5 m. Lastly, the bathymetry uncertainty
1662 component resulting from the prism densities is heterogeneous, with some spatially
1663 limited, but large values. The mean value is ~ 10 m, but some areas are up to 30
1664 m. There high uncertainties are strongly correlated with the error in the starting
1665 bathymetry (Figure 3.26b). This is due to the change in density contrast resulting
1666 in a change in the total bathymetry correction calculated in the inversion. In other
1667 words, the residual misfit can be minimized by a large surface correction with a low
1668 density contrast or a small surface correction with a large density contrast. The
1669 combined Monte-Carlo simulation (Figure 3.31a) shows the expected features of an
1670 uncertainty map. It has a baselevel uncertainty equal to the bouguer slab thickness

from the assumed gravity uncertainty, it is generally lowest at the constraints and highest in the large constraint gaps, and it is high where the inversion has produced a large change from the starting model.

3.10 Future work

Running this inversion with the various synthetic models gave us the ability to assess the inversion performance. From this assessment, we have determined several components which would benefit from additional investigation.

1. Test the effects of the relative strengths of the regional and residual components.
2. Implement an additional cross-validation to estimate the optimal density contrast, as in Uieda and Barbosa (2017). Here, we have used the same density contrasts for the creation of the observed gravity data and for the inversion itself. In a non-synthetic scenario, this contrast would need to be estimated.
3. Test the effects of flight line orientation relative to the dominant trend of geologic structures.
4. Implement a more robust method of enforcing the constraints points. This may likely be in the form of a bounded least squares solver or matrix math associated with the Jacobian.
5. Quantify the uncertainty of the regional separation process. This will likely include techniques used in conventional bathymetry surveying (Bourgeois et al., 2016; Calder & Elmore, 2017).
6. Include the equivalent source gridding of the observed gravity data in the Monte Carlo analysis to see the effects of the entire workflow, not just the inversion.
7. Perform a three-way comparison of the effects of constraint spatial density, gravity survey spacing, and gravity noise.
8. Testing the effects of pre-filtering the gravity data, either spatially or temporally, to remove the effects of noise.

3.11 Conclusion

With the goal of modelling the bathymetry beneath a floating ice shelf, we present a geometric gravity inversion which 1) adheres to prior bathymetry point measurements, within their uncertainties, 2) produces a smooth and realistic bathymetry, 3) accounts for the regional gravity field and 4) is computationally efficient and fully-open source. To demonstrate the effectiveness, as well as the limitations, we conducted a series of inversions using synthetic and semi-realistic data. These inversions showed the importance of accurately estimating and removing the regional component of gravity prior to the inversion. We showed that for the constraint arrangement for many Antarctic ice shelves, the optimal method for estimating this

1709 regional field is with a constraint-point minimization. In addition, we further ex-
1710 plored this method by testing various gridding (interpolation) techniques, and found
1711 the clear increase in performance when using a cross-validated bi-harmonic spline
1712 instead of the typically used tensioned minimum curvature.

1713

1714 Testing the various models with differing levels of gravity noise and number of
1715 gravity observation points highlights an important factor in planning a gravity sur-
1716 vey. We show for the Ross Sea synthetic model, which likely emulates the scenario
1717 expected from many Antarctic ice shelves, there are diminishing returns for average
1718 flight line spacings smaller than ~ 40 km, if the goal is to recover bathymetry with a
1719 5 km resolution. However, the inverted bathymetry's accuracy is strongly effected by
1720 noise in the gravity data. With this, the typically airborne survey focus on quantity
1721 of quality may need to be reassessed. If 40 km spaced flight lines produce similar
1722 results to 20 km lines, flying half the number of lines will save a significant amount of
1723 time. This time could be used to either expand the area of the survey or reduce the
1724 noise in the data. Reducing the data noise for an airborne survey may not always
1725 be feasible, but a few measures may be taken to attempt this, all of which are aided
1726 by the increased survey time allowed by reducing the numbers of flight lines. These
1727 include repeating lines or sections which are noisy, limiting flights to good weather
1728 windows, increasing the number of tie-lines, making shorter loops for base-station
1729 ties, or flying at lower altitudes and or ground-speeds.

1730

1731 The previous measurements of bathymetry, referred to as the constraints, are a
1732 vital part of an inversion for bathymetry. Due to the non-uniqueness of an inver-
1733 sion, there are an infinite number of inverted bathymetry models which will equally
1734 match the observed data. These constraints provide the ground truth necessary to
1735 confidently choose a model out of these infinite choices. Additionally, if not more
1736 importantly, they provide the primary method of accounting for the regional com-
1737 ponent of gravity. Since this is shown to be the largest source of uncertainty, the
1738 constraints are the most important aspect of the inversion. We tested the effects of
1739 varying the spatial density of the constraint points. The results (Figure 3.32) show
1740 the range of constraint point spacing's for the Ross Sea synthetic model which jus-
1741 tify conducting a gravity inversion, if the goal is to recover bathymetry with a 5 km
1742 resolution.

1743

1744 The optimal constraint spacing's are between $\sim 20\text{-}70$ km. Smaller spacing's al-
1745 ready have an adequate amount of information and little is gained over a simple
1746 interpolation of the data. At spacing's larger than ~ 70 km, the errors in estimating
1747 the regional field are larger than the improvements made by the inversion. These
1748 values, while specific to the Ross Sea scenario, provide an important context for
1749 the feasibility of conduct bathymetry inversions. Taken together with the above
1750 assessment on the relative importance of the gravity noise and density, some general
1751 guidelines are provided.

1752

1753 Constraints are the most important aspect on an bathymetry inversion. As long
1754 as the gravity data is on the order of magnitude of $2\text{-}4\times$ the spacing of the desired
1755 bathymetry resolution, and the noise levels are low, efforts should be focused on
1756 collecting more bathymetry measurements. The uncertainty of these depth mea-
1757 surements is relatively unimportant (Figure 3.31c), meaning quantity over quality is

1758 acceptable here. The final spatial uncertainty of the inverted bathymetry is strongly
1759 tied to the distance to the nearest constraint. This suggests that an even distribution
1760 of the constraints is important. However, if specific regions of the survey are
1761 expected to have larger amplitude regional anomalies, an increased spatial density
1762 of constraints over this region would be beneficial. With these recommendations, future
1763 planning for Antarctic fieldwork should be able to collect data which prioritizes
1764 the accurate assessment of sub-ice shelf bathymetry.

1765 Chapter 4 applies the inversion presented here to model the bathymetry beneath
1766 Antarctica's Ross Ice Shelf.